188. Pyranosyl-RNA ('p-RNA'): NMR and Molecular-Dynamics Study of the Duplex Formed by Self-pairing of Ribopyranosyl-(C-G-A-A-T-T-C-G)[1])

by **Irene Schlönvogt**[2]), **Stefan Pitsch**, **Catherine Lesueur**, **Albert Eschenmoser**, and **Bernhard Jaun***

Laboratorium für Organische Chemie, ETH-Zentrum, Universitätstrasse 16, CH–8092 Zürich

and **Romain M. Wolf***

Central Research Laboratories, *Ciba-Geigy Ltd.*, CH–4002 Basel

(17.X.96)

The solution structure of the duplex formed by self-pairing of the p-RNA octamer β-D-ribopyranosyl-(2′→4′)-(CGAATTCG) was studied by NMR techniques and, independently, by molecular-dynamics calculations. The resonances of all non-exchanging protons, H-bearing C-atoms, P-atoms, and of most NH protons were assigned. Dihedral angle and distance constraints derived from coupling constants and NOESY spectra are consistent with a single dominant conformer and corroborate the main structural features predicted by qualitative conformational analysis. The duplex displays *Watson-Crick* pairing with antiparallel strand orientation. The dihedral angles β and ε in the phosphodiester linkages differ considerably from the idealized values. Model considerations indicate that these deviations from the idealized model allow better *inter* strand stacking and lessen unfavorable interactions in the backbone. The average base-pair axis forms an angle of *ca.* 40° with the backbone. The resulting *inter* strand π-π stacking between either two purines, or a purine and a pyrimidine, but not between two pyrimidines, constitutes a characteristic structural feature of the p-RNA duplex. A 1000-ps molecular-dynamics (MD) calculation with the AMBER force field resulted in an average structure of the same conformation type as derived by NMR. For the backbone torsion angle ε, dynamically averaged coupling constants from the MD calculation agree well with the experimental values, but for the angle β, a systematic difference of *ca.* 25° remains. The two base pairs at the ends of the duplex are calculated to be highly labile, which is consistent with the high exchange rate of the corresponding imino protons found by NMR.

1. Introduction. – Our previous communications on the chemistry of pyranosyl-RNA (β-D-ribopyranosyl-(2′→4′)-oligonucleotides) [1–3] described pairing studies demonstrating that this isomer of natural RNA, which contains six-membered instead of five-membered ribose rings and 4′→2′ instead of 5′→3′ phosphodiester linkages, constitutes a new pairing system exhibiting strong and highly selective purine-pyrimidine pairing.

p-RNA is the fourth potentially natural nucleic-acid alternative that has been synthesized and studied at the ETH in the context of experimental investigations directed towards a chemical etiology of nucleic-acid structure [4] [5]. It has been predicted to constitute an efficient *Watson-Crick* pairing system on the basis of qualitative conformational analysis [2] [4], which led to the conclusion that, among the 162 idealized conformations of a p-RNA backbone unit to be considered, only one fulfills the conformational selection rule [4] for base pairing in an oligomer.

---

[1]) 4th Communication in the series 'Pyranosyl-RNA ('p-RNA')'. For the 3rd communication, see [1].

[2]) Part of the planned Ph. D. thesis of *I. S.*

This pairing conformation contains (idealized) ribopyranose chairs with the nucleobase and phosphodiester groups in equatorial positions. The phosphodiester linkages have *gauche-trans*-conformation with torsion angles as shown in *Fig. 1*. Translational repetition of such an idealized backbone unit leads to a strictly linear single strand. Model considerations predict that, upon pairing, such linear strands assume a *quasi*-linear duplex structure with *Watson-Crick* pairing. As a consequence of the large inclination between the backbone and (average) base-pair axis (*ca.* 45°), a predominance of *inter*-strand as opposed to *intra*strand base stacking, as well as a strictly antiparallel strand orientation are expected.

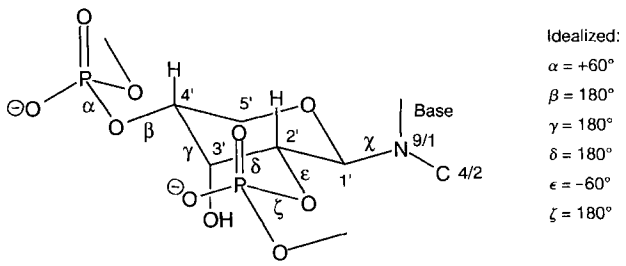

Fig. 1. *Pairing conformation of p-RNA (idealized)*. Atom numbering and definition of torsional angles for p-RNA correspond to the standard IUPAC nomenclature for nucleic acids [14]:
Backbone: ... O2′(i − 1)–P-α-O4′-β-C4′-γ-C3′-δ-C2′-ε-O2′-ζ-P-O4′(i + 1) ...
Base: ... C4-N9-χ-C1′–O5′ ... in purines; ... C2–N1-χ-C1′–O5′ ... in pyrimidines.

The results of the experimental studies described in [1–3] so far corroborate these predictions. In particular, the high pairing selectivity, *i.e.*, the exclusive observation of *Watson-Crick* and the (so far) complete absence of *Hoogsteen*- and reverse-*Hoogsteen* pairing in this series, can be rationalized on the basis of the idealized conformational model (*Fig. 1*). In the absence of experimentally derived structural data, however, it remained unknown, to what extent and in which respects the actual solution conformation of a p-RNA duplex deviates from the idealized model.

Here, we report on the first NMR-spectroscopic study of a p-RNA duplex, the self-paired octamer [β-D-ribopyranosyl-(2′→4′)-(CGAATTCG)]$_2$ (**1**), and compare the results with the idealized conformational model on one hand, and with the average structure generated by a molecular-dynamics calculation of the same duplex on the other hand.

The sequence pr-CGAATTCG (pr = ribopyranosyl) was selected and synthesized for the purpose of this study, because it was expected to show strong pairing while offering sufficient sequential variation to reduce the problem of spectral overlap, which had hampered earlier NMR studies of homo-DNA oligonucleotides such as ddGlc(AAAAATTTTT) [6] and ddGlc(AGAGAG) [7] [8].

The NMR study and molecular-dynamics (MD) calculations were carried out independently of each other. Thus, in contrast to the more common procedure [9–12], no NMR-derived distance and angle constraints were used for the calculations. This unbiased approach was preferred, because it was not known *a priori*, whether the standard AMBER force field would be able to predict the conformations and dynamics of a new

oligonucleotide constitution such as p-RNA correctly. The comparison of the NMR-derived structural parameters with the results of the MD calculations, which will be discussed below, is both a test of the computational method and an attempt to understand the dynamics of p-RNA duplexes, on which only very limited information could be obtained by NMR.

2. NMR Spectroscopy of pr-CGAATTCG. – *Assignments and Proof of Constitution.* ^{1}H- and ^{31}P-NMR spectra of **1** (*ca.* 5.3 mM in D_2O, 0.05M sodium arsenate, pH 7.4), recorded at temperatures between 0° and 50°, showed that both the line-widths and the ^{31}P-dispersion were optimal at 25°. This is in contrast to the homo-DNA decanucleotide [6] where the lines were found to be more narrow at 50° than at 25°.

The observation of seven resolved lines in the $\{^1H\}$-decoupled ^{31}P-NMR spectrum and the number of lines in the $\{^1H\}$-broad-band-decoupled ^{13}C-NMR spectrum are consistent with either a duplex exhibiting C_2 symmetry on the NMR time scale or a single strand. The latter possibility can be excluded, because the estimated melting point of *ca.* 87° (extrapolated from UV and CD studies in the concentration range of 3–18 μM), and the observed *inter*strand NOEs (see below) establish that **1** is paired at the concentration of the NMR sample (*ca.* 5.3 mM). An overview of the full ^{1}H-NMR spectrum of **1** in D_2O is shown in *Fig. 2*.

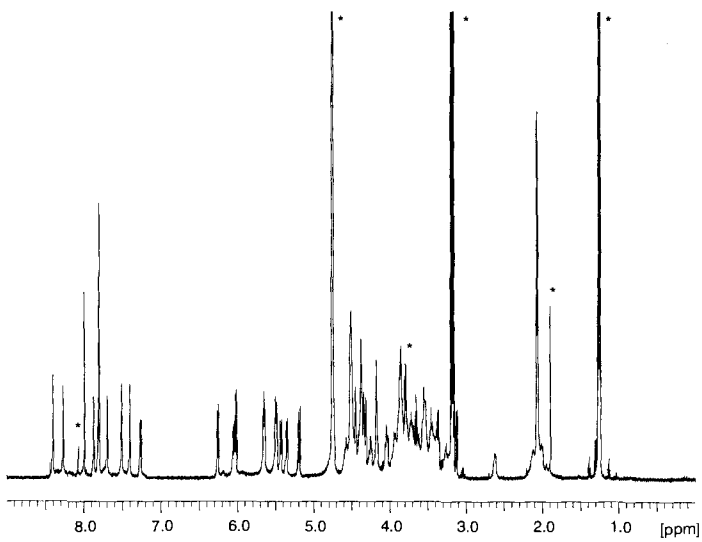

Fig. 2. *500-MHz ^{1}H-NMR Spectrum of* **1** *in D_2O* (6.4 mg in 0.4 ml D_2O, 0.05M sodium arsenate, 25°; lines due to solvent and impurities are labeled with *)

All proton signals of the eight sugar rings could be assigned through TOCSY, DQF.COSY, and, in the case of the $CH_2(5')$ protons, HSQC spectra. The signals of the anomeric protons are well dispersed. Strong spectral overlap was observed in the region from 4.5 to 4.3 ppm, where most of the H–C(2′) and H–C(3′) resonances appear, and in the region between 3.8 and 3.3 ppm containing the H–C(4′) and $CH_2(5')$ signals. Whereas

the chemical shift of all sugar protons could be determined, a few signals were practically isochronous, which made the assignment of the corresponding cross peaks in the NOESY spectra ambiguous and prevented their use for distance estimation.

The sequential assignment of the eight pyranose spin systems followed from the [^{1}H,^{31}P]-COSY spectrum shown in *Fig. 3*. The ^{31}P-resonance of each phosphodiester unit shows cross peaks to H–C(2′) of the pyranose ring preceding it and to H–C(4′) of the one following it in the sequence.

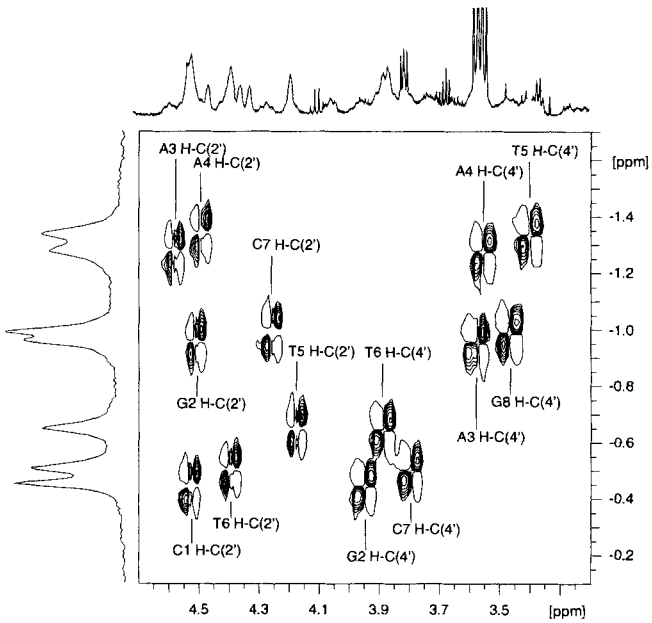

Fig. 3. *^{1}H,^{31}P-COSY Spectrum of* **1** *in D_2O* (conditions: see *Exper. Part*)

Since the 2D-NMR methods used here do not provide scalar correlations between the sugar protons and the aromatic protons of the attached base, the assignments of the latter were deduced from strong *intra*-residue NOESY cross peaks between the H–C(8/6) proton of the base, and H–C(2′) and H–C(4′) of the attached ribopyranose (*cf. Fig. 5*). The assignments of the thymidine Me groups and of the cytidine H–C(6) protons followed from scalar correlations (long range in the case of Me–C(6)). The full analysis of the *intra*- and *inter*strand NOE pattern (see below) eventually led to the assignment of the adenine H–C(2) protons and – from the NOESY spectra of **1** in H_2O/D_2O 9:1 – of most of the exchangeable protons.

The chemical shifts of all assigned protons are compiled in *Table 1*, those of the proton-bearing C-atoms and of all P-atoms in *Table 2*. Together, the shift correlation spectra prove that β-D-ribopyranosyl-(2′→4′)-(CGAATTCG) has been synthesized without rearrangements or errors in the sequence.

Table 1. *^{1}H-NMR Chemical Shifts and Assignments*

	H–C(1′)[a])	H–C(2′)[a])	H–C(3′)[a])	H–C(4′)[a])	H_{ax}–C(5′)[a])	H_{eq}–C(5′)[a])	Me–C(5)[b])
C1	6.05	4.53	4.53	4.04	3.85	3.82	
G2	5.50	4.51	4.51	3.95	3.87	3.72	
A3	5.50	4.58	4.38	3.57	3.55	2.62	
A4	5.36	4.50	4.35	3.55	3.27	2.13	
T5	5.43	4.18	4.32	3.40	3.21	2.01	2.08
T6	5.65	4.39	4.45	3.89	3.77	3.54	2.06
C7	5.66	4.26	4.38	3.80	3.72	3.43	
G8	5.19	3.85	4.18	3.46	3.62	3.38	
	H–C(2)[b])	H–C(8)[b])	H–C(5)[c])	H–C(6)[c])	NH_2[d])	NH(1)[d])	NH(3)[d])
C1			6.26	7.81	7.61, 8.3[e])		
G2		7.87			6.69	12.58	
A3	7.80	8.27			6.91		
A4	7.99	8.40			7.36		
T5				7.51			14.14
T6				7.41			13.46
C7			6.02	7.27	8.09[f]), 7.22		
G8		7.70			6.34		

[a]) Assignment based on COSY and TOCSY. [b]) Assignment based on NOESY. [c]) Assignment based on COSY and NOESY. [d]) Assignment based on NOESY in H_2O/D_2O 90:10. [e]) Tentative assignment. [f]) H-Bonded proton.

Table 2. *^{13}C- and ^{31}P-NMR Chemical Shifts and Assignments*

	C(1′)[a])	C(2′)[a])	C(3′)[a])	C(4′)[a])	C(5′)[a])	C(2)[a])	C(8)[a])	C(5)[a])	C(6)[a])	Me[a])	^{31}P[b])
C1	81.6	74.1	72.7	68.5	67.9			100.7	144.1		−0.45
G2	80.0[c])	75.2	71.8	73.0	65.5		138.2[d])				−0.96
A3	79.8[d])	74.7	71.8	72.7	64.5	154.7	142.3				−1.27
A4	79.6[d])	74.6	71.7	72.6	64.3	155.3	142.9				−1.34
T5	80.7	73.1	71.8	72.4	65.1				140.9	14.8	−0.65
T6	81.0	73.3	72.0	73.1	65.2				140.4	14.8	−0.50
C7	81.4	74.1	72.1	73.3	65.1			100.5	143.7		−0.99
G8	81.0	70.7	72.7	73.0	65.1		139.1				

[a]) Assignment based on HSQC. [b]) Assignment based on [H,P]-COSY. [c]) Assignment uncertain (^{13}C-resonances nearly isochronous). [d]) Assignment uncertain (low cross-peak intensity).

Homo- and Heteronuclear Coupling Constants (Conformation of the Backbone). Of the six dihedral angles that specify the backbone of RNA, four (β, γ, δ, ε; see *Fig. 1*) can, in principle, be determined by NMR through measurement of vicinal ^3J(H,H), ^3J(H,P), and ^3J(C,P) coupling constants, and application of appropriate *Karplus* relations.

Since the experimental values of coupling constants correspond to the weighted time average over all populated conformations, a consistent picture allowing interpretation in terms of a single structure will only be obtained, if a single conformer dominates the equilibrium. Although the high melting point, the sharp NMR signals at room temperature, and the relatively slow exchange of imino protons (see below) all point to a strongly paired, well-defined solution structure of the duplex, the possibility that more than one

conformer is significantly populated has to be considered[3]). The fact that the analysis of the NMR data discussed below, which is based on the hypothesis that a single conformation type dominates, leads to consistent structural parameters justifies this assumption *a posteriori*.

Whereas $^3J(1',2')$ and $^3J(P,C)$ could be determined directly from the 1D spectra, all $^3J(H,P)$ and most $^3J(H,H)$ values had to be extracted from 2D spectra by iterative fitting of calculated curves to 1D traces through cross peaks of DQF.COSY spectra acquired with and without $\{^{31}P\}$ decoupling (see *Exper. Part*). Due to the lower S/N ratio and possible errors in line-width determination, the precision of coupling constants from 2D spectra is lower than of those from 1D spectra. All determined values are collected in *Table 3*.

Table 3. *Homo- and Heteronuclear Coupling Constants*

	$J(1',2')^a)$	$J(1',2')^b)$	$J(3',4')^b)$	$J(4',5'_{ax})^b)$	$J(4',5'_{eq})^b)$	$J(2',P)^b)$
C1	9.3 ± 0.2		3.5 ± 1	10.2 ± 1	6.3 ± 1	7.2 ± 0.5
G2	8.7 ± 0.4	8.4 ± 0.5	3.5 ± 1	9.7 ± 1	5.6 ± 1	6.9 ± 0.5
A3	9.1 ± 0.2	9.3 ± 0.5				7.4 ± 0.5
A4	9.0 ± 0.2	9.5 ± 0.5				7.8 ± 0.5
T5	9.0 ± 0.2	9.5 ± 0.5	3.5 ± 1	9.7 ± 1	5.6 ± 1	7.1 ± 0.5
T6	9.0 ● 0.2	9.3 ± 0.5	3 ± 1	10 ± 1	5.3 ± 1	7.4 ± 0.5
C7	9.1 ± 0.2	9.2 ± 0.5	3 ± 1	9.5 ± 1	5 ± 1	8.3 ± 0.5
G8	9.6 ± 0.2	9.8 ± 0.5	3 ± 1	9.7 ± 1	5.4 ± 1	
	$J(4',P)^b)$	$J(C(1'),P)^c)$	$J(C(2'),P)^c)$	$J(C(3'),P)^c)$	$J(C(4'),P)^c)$	$J(C(5'),P)^c)$
C1		11 ± 0.5	4 ± 1			
G2	10 ± 1	11 ± 0.5	4 ± 1			3.1 ± 0.5
A3		11 ± 0.5	4 ± 1			3.1 ± 0.5
A4		11 ± 0.5	4 ± 1	8 ± 1		3.1 ± 0.5
T5	10 ± 1	11.2 ± 0.5			4 ± 1	
T6	9 ± 1	9.5 ± 0.5		8 ± 1		
C7	9 ± 1	9.5 ± 0.5	4 ± 1	8 ± 1		
G8	10.5 ± 1					

[a]) Determined by fitting of 2 *Lorentz* lines to the proton 1D spectrum. [b]) Determined by fitting of *Gauss* lines to traces of COSY spectra with/without $\{^{31}P\}$ decoupling. [c]) Determined by fitting of 2 *Lorentz* lines to the broad-band-decoupled ^{13}C spectrum.

Considering the rather large error limits, the observed variation of coupling constants along the sequence is too small to allow interpretation as sequence-dependent conformational differences. For the following discussion, it will, therefore, be assumed that the conformation of all backbone units along the sequence is qualitatively the same.

The coupling constants $^3J(H,H)$ within the six-membered pyranose ring are close to the values for N-glycosides of β-D-ribopyranose (assigned to the pure chair conformation by *Altona* and *Haasnoot* [13]) and to those found in single strand pr-A_3 [2]. Compared to these reference structures, **1** exhibits slightly lower diaxial coupling constants and slightly higher axial-equatorial ones. Whether the minor differences are due to

[3]) In the case of the homo-DNA duplex ddGlc(AAAAATTTTT), the NMR analysis led to the conclusion that two conformation types were significantly populated at 50° [6].

a slight flattening of the chair or to the admixture of non-chair pyranose conformations ($< 5\%$) can not be decided from the NMR data. Qualitatively, the results show that the endocyclic dihedral angles γ and δ in the solution structure of **1** are close to those of the idealized conformation ($\gamma = \delta = 180°$).

The dihedral angles around the exocyclic C–O bonds in the phosphodiester linkages are reflected in the coupling constants $^3J(4',P(4'))$, $^3J(C(3'),P(4'))$, and $^3J(C(5'),P(4'))$ for β, and $^3J(2',P(2'))$, $^3J(C(3'),P(2'))$, and $^3J(C(1'),P(2'))$ for ε. *Karplus* relations for $^3J(P,H)$ and $^3J(P,C)$ are available from the literature, but the parameters proposed by different authors, in particular for $^3J(C,P)$, differ considerably [10]. Furthermore, it was not clear at the outset of this study whether the *Karplus* parameters that have been determined and successfully used for native DNA and RNA would be applicable to the p-RNA constitution as well. This prompted us to test the proposed sets of *Karplus* parameters on three cyclophosphates of β-D-ribopyranose-nucleosides (**2–4**; see *Exper. Part*) by comparing the experimentally determined coupling constants with those predicted by molecular-mechanics calculations. Since for all three compounds good agreement was obtained with the *Karplus* relations proposed by *Wijmenga et al.* [10], this set of parameters was selected for the following analysis.

The value of 9.5 ± 1 Hz observed for $^3J(4',P(4'))$ is consistent with four ranges of the angle β: ($+136° \pm 5°$), ($104° \pm 5°$), ($-2° \pm 3°$), and ($-117° \pm 3°$). Combination with the four dihedral angles corresponding to $^3J(C(5'),P(4')) = 3.1 \pm 1$ Hz and the two possibilities for $^3J(C(3'),P(4')) = 8 \pm 1$ Hz shows that only $\beta = 145 \pm 6°$ is compatible with all three coupling constants[4]).

The experimental values of the coupling constants $^3J(2',P(2'))$, $^3J(C(3'),P(2'))$, and $^3J(C(1'),P(2'))$ are consistent with a single solution: $\varepsilon = -85 \pm 5°$. Although vicinal to two P-atoms, C-atom C(3′) exhibits only one resolved coupling of 8 ± 1 Hz, which implies that one of its $J(C,P)$ couplings must be smaller than the line-width (< 1.5 Hz). Since dihedral angles of $\pm 85°$, which would be consistent with $^3J(C,P) = 1.5$ Hz, are incompatible with the other two couplings to P(4′), the assignment of the 8-Hz splitting to $^3J(P(4'),C(3'))$ and, by consequence, $^3J(P(2'),C(3')) \leq 1.5$ Hz was straightforward.

The experimentally derived average dihedral angles shown in *Fig. 4* deviate significantly from the idealized backbone conformation (*Fig. 1*). Since the torsional angles α and ζ are not accessible by NMR techniques, interpretation of the consequences of these deformations to the duplex conformation has to rely in part on model considerations. Adjusting ε from $-60°$ (idealized) to $-85°$ (NMR), and β from $180°$ to $+145°$ requires simultaneous adjustments of α from $60°$ to *ca.* $70°$, and of ζ from $180°$ to *ca.* $-170°$ in order to maintain the pairing propensity of single strands[5]). In the resulting NMR-consistent model conformation, the unfavorable interactions between O–C(2′) and H_{eq}–C(5′) on one hand and between H–C(3′) and one of the phosphate O-atoms on the other hand are considerably reduced compared to the idealized model (the distances increase from

---

[4]) The modified parametrization proposed more recently in [14] leads to a curve that deviates from that of *Wijmenga et al.* [10] in the region of $\varphi < 90°$. Assuming the validity of this modification, a second solution for our experimental ^3J values exists ($\beta = -10 \pm 6°$). However, this possibility can be excluded, because, together with $\varepsilon = -85 \pm 5°$, it would correspond to a backbone that folds back onto itself within three residues and would be incompatible with pairing.

[5]) These values for α and ζ were also obtained by energy minimization (AMBER) of the idealized conformation of the duplex **1**, if the torsional angles β and ε were constrained to the NMR-derived values.

ca. 3 Å to *ca.* 4 Å). Possibly even more important consequences are a reduction of the π-π stacking distance from over 4 Å in the idealized model to *ca.* 3.5 Å, and an improvement of *inter*strand stacking through increased inclination of the average base pair axis against the backbone axis (see below).

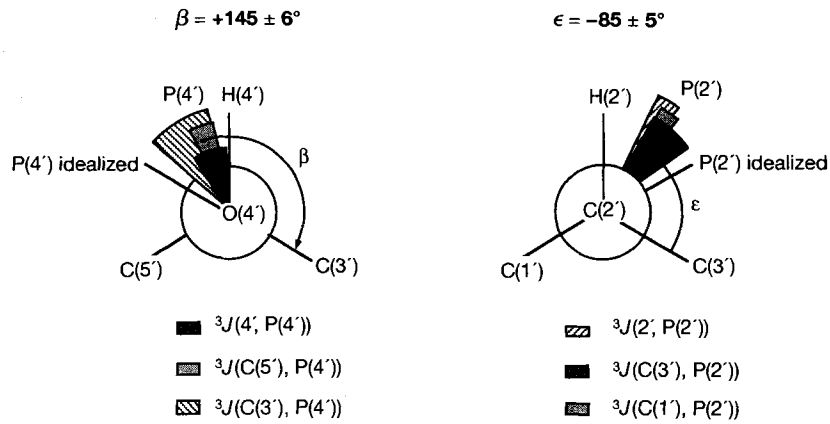

Fig. 4. *Backbone angles β and ε derived from coupling constants.* The drawn sectors correspond to the range of coupling constants observed for individual residues plus the estimated experimental errors.

NOESY Spectroscopy of Non-exchangeable Protons in D_2O (Glycosidic Torsion Angle χ, Proof of Pairing and of Antiparallel Strand Orientation, Inclination of Base-Pair Axis). A series of NOESY spectra with mixing times of 40, 60, 80, and 150 ms but otherwise identical parameters was acquired. To check for spin diffusion, a ROESY spectrum (t_m = 150 ms) was measured as well. Relative distances were estimated by integration of NOESY cross peaks and construction of NOE build-up curves. The significant NOESY cross peaks are listed in *Table 4* grouped into the categories weak (w), medium (m) and strong (s).

Table 4. *NOE Correlations of Non-exchangeable Protons*

Proton	Cross-peak to	Intensity[a])	Proton	Cross-peak to	Intensity[a])
C1 H–C(1′)	C1 H_{ax}–C(5′)	s	A4 H–C(8)	A4 H–C(2′)	s
	C1 H_{eq}–C(5′)	m		A4 H–C(4′)	w
C1 H–C(2′)	C1 H–C(4′)	s	A4 H_{ax}–C(5′)	A4 H_{eq}–C(5′)	s
C1 H–C(6)	C1 H–C(2′)	s	T5 H–C(1′)	T5 H_{ax}–C(5′)	s
	C1 H–C(4′)	w		T5 H_{eq}–C(5′)	m
	C1 H–C(5)	s		T6 H_{ax}–C(5′)	w
G2 H–C(1′)	G2 H_{eq}–C(5′)	m		T6 H_{eq}–C(5′)	m
G2 H–C(2′)	G2 H–C(4′)	s	T5 H–C(6)	T5 H–C(2′)	s
G2 H–C(8)	G2 H–C(2′)	s		T5 H–C(4′)	w
	G2 H–C(4′)	w	T5 H_{ax}–C(5′)	T5 H_{eq}–C(5′)	s
A3 H–C(1′)	A3 H_{eq}–C(5′)	m	T6 H–C(1′)	T6 H_{eq}–C(5′)	m
	A4 H_{ax}–C(5′)	w	T6 H–C(2′)	T6 H–C(4′)	s
	A4 H_{eq}–C(5′)	m	T6 H–C(6)	T6 H–C(4′)	w
A3 H–C(2′)	A3 H–C(4′)	s		T6 H–C(2′)	s

Table 4 (cont.)

Proton	Cross-peak to	Intensity[a])	Proton	Cross-peak to	Intensity[a])
A3 H–C(2)	A3 H–C(1′)	w	T6 H_{ax}–C(5′)	T6 H_{eq}–C(5′)	s
	A4 H_{eq}–C(5′)	w	C7 H–C(1′)	C7 H_{eq}–C(5′)	s
	C7 H–C(1′)	w		G8 H_{eq}–C(5′)	w
	C7 H_{ax}–C(5′)	w	C7 H–C(2′)	C7 H–C(4′)	s
	C7 H_{eq}–C(5′)	w	C7 H–C(6)	C7 H–C(2′)	s
A3 H–C(8)	A3 H–C(2′)	s		C7 H–C(4′)	w
	A3 H–C(4′)	w		C7 H–C(5)	s
A4 H–C(1′)	A4 H_{ax}–C(5′)	s	C7 H_{ax}–C(5′)	C7 H_{eq}–C(5′)	s
	A4 H_{eq}–C(5′)	m	G8 H–C(1′)	G8 H_{ax}–C(5′)	s
	T5 H_{eq}–C(5′)	m		G8 H_{eq}–C(5′)	m
A4 H–C(2′)	A4 H–C(4′)	s	G8 H–C(2′)	G8 H–C(4′)	s
A4 H–C(2)	A4 H–C(1′)	w	G8 H–C(8)	C7 H–C(5)	w
	T5 H–C(1′)	w		G8 H–C(2′)	s
	T5 H_{eq}–C(5′)	w		G8 H–C(4′)	w
	T6 H–C(1′)	w	G8 H_{ax}–C(5′)	G8 H_{eq}–C(5′)	s
	T6 H_{ax}–C(5′)	w			
	T6 H_{eq}–C(5′)	w			

[a]) Estimated distance range: s: < 2.5 Å, m: 2.5–3 Å, w: > 3 Å.

Comparison of initial NOE build-up rates for the cross-peaks H–C(6/8)→H–C(2′) and H–C(6/8)→H–C(4′), in principle, allows to estimate the ratio of the two corresponding distances and, with the conformation of the pyranose rings being close to an ideal chair, the dihedral angle χ.

The relevant section of the NOESY spectrum is shown in *Fig. 5*. Because cross-peaks to H–C(4′) were found to be affected by spin diffusion at mixing times above 40 ms, the error in the determination of χ by this method is rather large (*ca.* ±8°). For all residues, with the exception of G8 and A4, values of χ between −120° and −135° (*anti*) were determined. For residue A4, χ was calculated to be *ca.* −110°, a deviation that is close to the estimated error limit, but may signify either a change in the base-stacking geometry or increased conformational mobility in the middle of the sequence. In residue G8, H–C(8) appears to be much nearer to H–C(2′) than to H–C(4′) (formally, a value of $-105° < \chi < -90°$ was calculated). However, this difference in the apparent torsional angle χ could also be the result of higher conformational mobility of the last base pair in the duplex, an interpretation which is supported by the molecular-dynamics calculations (see below).

Along the sugar-phosphodiester backbone, an uninterrupted chain of NOEs $H–C(1')_n \rightarrow H_{ax}–C(5')_n \rightarrow H_{eq}–C(5')_n \rightarrow H–C(1')_{n+1}$ was observed (*Fig. 6*). Based on a 1,3-diaxial distance of 2.36 Å between the $H–C(1')_n$ and $H_{ax}–C(5')_n$ protons in the pyranose ring, NOE Build-up curves lead to estimates for the *inter*-pyranose distance $H_{eq}–C(5')_n \rightarrow H–C(1')_{n+1}$ varying between 3.6 and 4.0 Å. This corresponds to a translational step of 6.5–6.9 Å from one pyranose unit to the next one along the backbone, which is consistent with the dihedral backbone angles determined from coupling constants and slightly lower than the value predicted for the idealized conformation (*ca.* 6.8 Å).

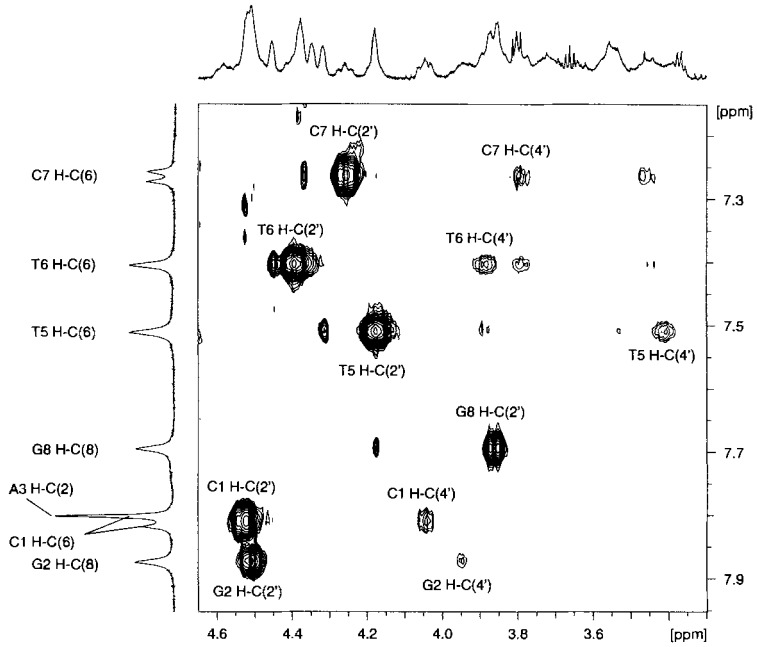

Fig. 5. *Expansion of the NOESY spectrum* (t_m = 80 ms) *of* **1** *in* D_2O *containing the cross-peaks between aromatic H–C(6/8) protons and pyranose H–C(2′) and H–C(4′) protons.* Conditions: see *Exper. Part.*

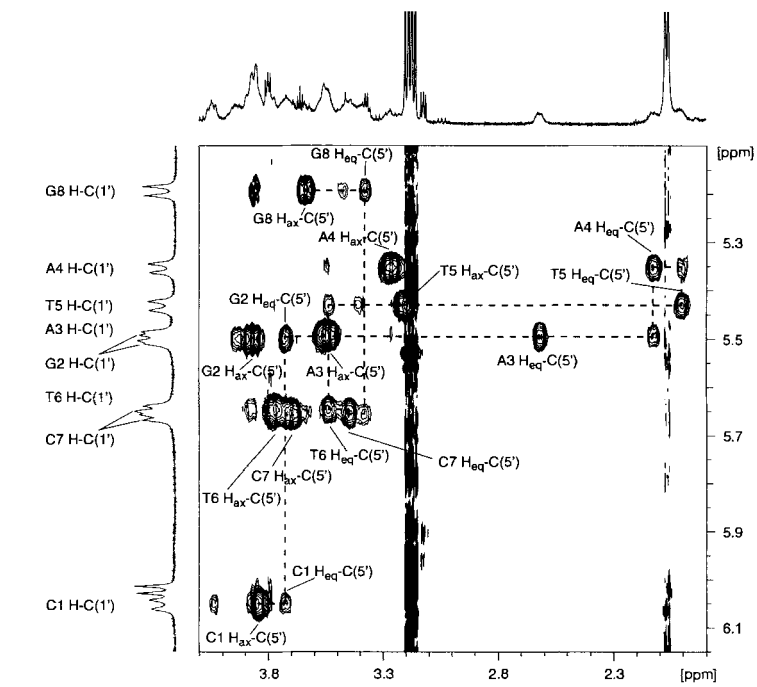

Fig. 6. *Expansion of the NOESY spectrum* (t_m = 80 ms) *of* **1** *in* D_2O. The broken line connects the cross-peaks corresponding to the sequence $H–C(1')_n \rightarrow H_{ax}–C(5')_n \rightarrow H_{eq}–C(5')_n \rightarrow H–C(1')_{n+1}$. Conditions: see *Exper. Part.*

The adenine H–C(2) protons show NOEs to the pyranose protons H–C(1′) and CH_2(5′) of the next nucleoside in the same strand, *and* to H–C(1′) and CH_2(5′) of the nucleoside following the pairing partner in the opposite stand (*Figs. 7* and *8*). As judged from the NOE data, the protons H–C(1′) and H_{eq}–C(5′) (*inter*- and *intra*strand) are at comparable mean distances from the adenine H–C(2) proton, which, therefore, must be situated close to the middle of the shallow groove on the concave[6]) side of the duplex. The observation of *inter*strand NOEs between adenine H–C(2) and pyranose protons not only proves the antiparallel pairing of **1**, but allows to define the angle between the (average) axis of the base pairs and the axis of the backbone (Φ in *Fig. 8*) quite narrowly. Assuming 2.36 Å for the 1,3-diaxial distance between H–C(1′) and H_{ax}–C(5′), the distances *a*, *b*, *c*, and *d* in *Fig. 8* are all estimated to be in the range from 3.9 to 4.4 Å. Because distances derived by using the two spin approximations are normally underestimated, especially for long distances [15] [16], these values constitute lower limits for *a*, *b*, *c*, and *d*. An upper limit is established by the observation that the *intra*nucleosidic NOEs between adenine H–C(2)$_n$ and adenine H–C(1′)$_n$ (distance *e* in *Fig. 8*) are consistently weaker than those corresponding to distances *a*, *b*, *c*, and *d*. Distance *e* is determined by the constitution of the purine base and the parameters of the glycosidic bond. For the NMR-derived χ values, this reference distance lies between 4.5 and 4.7 Å. Based on the constraints derived above, the average angle Φ must be smaller than 45° and larger than 35°.

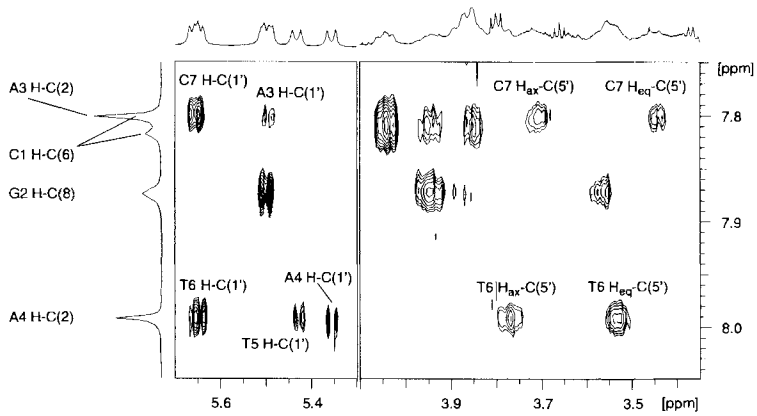

Fig. 7. *Expansion of the NOESY spectrum* (t_m = 150 ms) *of* **1** *in* D_2O *containing the* intra- *and* inter*strand cross-peaks between adenine H–C(2) protons and pyranose H–C(1′) and* H_{eq}*–C(5′) protons*

[6]) The definition of the *concave* and *convex* faces of the *quasi*-linear p-RNA duplex are shown below. Constitutionally, the concave side of p-RNA corresponds to the minor groove, the convex side to the major groove of *Watson-Crick*-paired natural DNA.

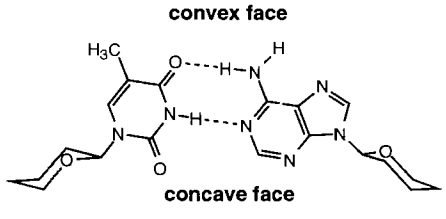

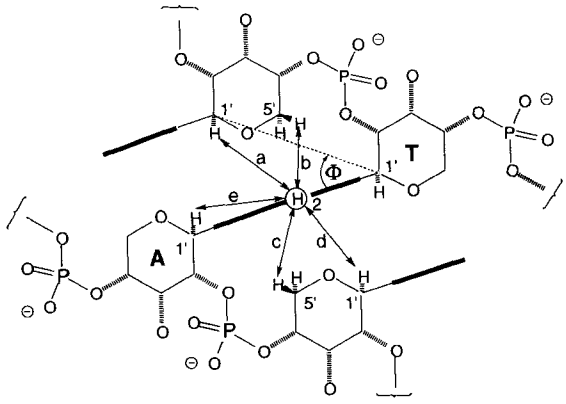

Fig. 8. Intra- *and* inter*strand distances* a–e *from adenine H–C(2) defining the angle Φ* (schematic drawing) *between the average base-pair axis and the backbone*

The extraordinary chemical shift of the protons H_{eq}–C(5) of the three inner nucleotides A3, A4, and T5 (see *Table 1*) constitutes independent evidence for a strong inclination of the average base-pair axis towards the backbone. Since these protons belong to the sugar rings that follow purine nucleotides in the sequence, their strong upfield shift must be due to the ring current of the adjacent purine bases. However, the determination of the mean position of the protons H_{eq}–C(5′) relative to the purine frame using published theoretical ring-current diagrams [17] [18] is difficult, because the reference chemical shift, and, therefore, the magnitude of the induced upfield shift, are unknown[7]). For equivalent positions relative to the aromatic ring, pyrimidine bases induce a much smaller upfield shift than purine bases. By taking the chemical shift of protons H_{eq}–C(5′) adjacent to pyrimidines as reference for 'unshifted' protons, a very conservative lower limit for the purine-induced shifts ($\Delta\delta_P$) is obtained. For proton T5 H_{eq}–C(5′), *e.g.*, this results in a lower limit of $\Delta\delta_P \geq 1.4$ ppm. According to the *iso*-shielding curves calculated by *Giessner-Prettre* and *Pullman* for adenine [18], such high values are expected only if the projection of the proton onto the aromatic plane is within a radius of *ca.* 1.2 Å from the *iso*-shielding maximum (close to the center of the C(4)–C(5) bond), *and* if the distance normal to the plane of the base is 3.4 Å or less. Since our estimate of the high-field shift of the three protons H_{eq}–C(5′) is a lower limit, the average distance between the protons H_{eq}–C(5′) and the plane of the adjacent purine base must be in the range between 2.6 and 3.2 Å.

NOESY Spectroscopy of Exchangeable Protons in H_2O/D_2O 9:1 (Pairing Mode, Inclination of Base-Pair Axis). Comparison of the low-field section of the 1D ^{1}H-NMR spectrum of **1** in H_2O/D_2O 9:1 (*Fig. 9, b*) with the corresponding spectrum in D_2O (*Fig. 9, a*) allowed to identify 10 out of the 16 possible NH signals. In the region from 14.5

[7]) Proton H_{eq}–C(5′) of the 4′-terminal residue C1 is unsuitable as a reference, because it not only lacks the adjacent base but the neighboring phosphodiester group as well. All H_{eq}–C(5′) protons, except the one at the 4′-end, are expected to be shifted upfield because of the contact with O–C(2′) of the phosphodiester linkage in the NMR-derived backbone conformation.

to 12 ppm, where the four imino proton resonances are expected, only three sharp lines were found. Seven broadened but still well-defined signals were located in the region from 8.2 to 6 ppm, where the 12 amino resonances would be expected.

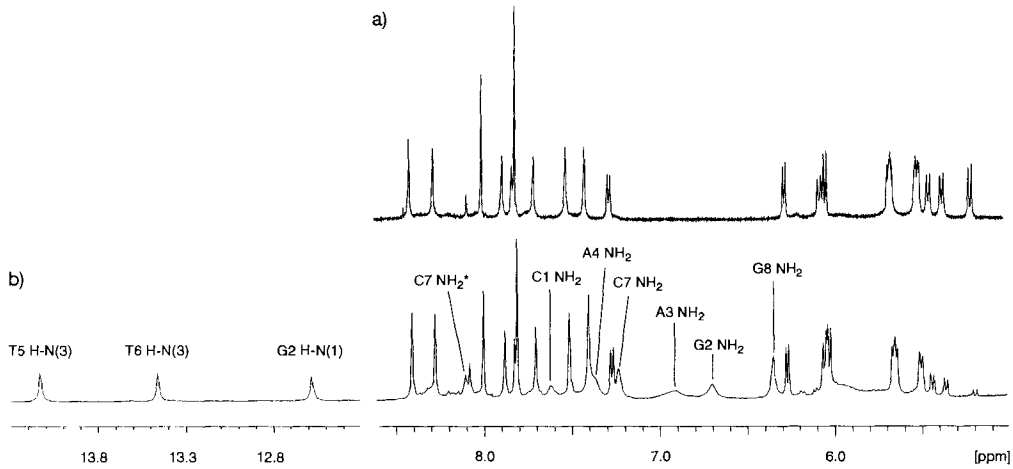

Fig. 9. *Low-field region of the 500-MHz ^{1}H-NMR spectra of* **1** *in* a) D_2O, b) H_2O/D_2O *9:1* (WATERGATE H_2O suppression, conditions: see *Exper. Part*). Resonances of slowly exchanging protons are labeled with their assignment. Cytidine-NH_2 protons are labeled with * for the hydrogen bound proton.

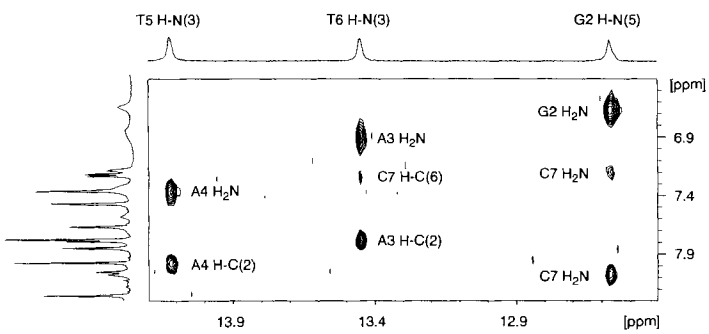

Fig. 10. *Expansion of the NOESY spectrum* (t_m = 80 ms, WATERGATE H_2O suppression) *of* **1** *in* H_2O/D_2O *9:1 containing the cross-peaks of imino protons* (top trace) *with the aromatic and exchangeable protons*. Conditions: see *Exper. Part*.

The assignment of the slowly exchanging protons was achieved through NOESY spectra (mixing times of 80 ms and 150 ms) acquired in H_2O/D_2O with WATERGATE water suppression to avoid saturation transfer. *Fig. 10* shows a section of the NOESY spectrum containing the cross-peaks between the three imino signals on one hand and adenine H–C(2) and amino NH signals on the other hand. Due to the strong NOE to the corresponding adenine H–C(2), the signals at 14.14 and 13.46 ppm could be assigned to the T5 and T6 imino protons, respectively. The imino signal at 12.58 ppm exhibits NOEs with three exchangeable protons which, based on their NOEs with non-exchangeable protons, all

belong to the C7–G2 base pair. Each of the T5 and T6 imino resonances shows one NOE with one amino signal, which was assigned to the corresponding adenine amino NH. Finally, two resonances at 7.61 and 6.34 ppm were assigned to amino protons of the C1–G2 base pair through NOEs to protons C1 H–C(5), C1 H–C(1′), and G2 H_{eq}–C(5′). Chemical shifts and assignments of the slowly exchanging NH resonances are compiled in *Table 1*, the significant NOESY cross-peaks of exchangeable protons are listed in *Table 5*. The pattern of NOEs between exchangeable protons [11] and their sequence-consistent correlations with non-exchangeable protons leave no doubt that, throughout the sequence, the pairing mode is of the *Watson-Crick* type.

Table 5. *NOE Correlations of Exchangeable Protons*

Proton[a])	Cross-peak to[a])	Intensity	Proton[a])	Cross-peak to[a])	Intensity
C1 H_2N^o	C1 H–C(5)	m	T6 HN	A3 H–C(2)	m
	A3 H–C(8)	m		A3 H_2N	m
G2 HN	G2 H_2N	s		T5 H–C(6)	w
	C7 H_2N^*	m		T6 H–C(1′)	w
	C7 H_2N^o	w		T6 H_3C–C(5)	w
	G8 H_{eq}–C(5′)	w		C7 H–C(6)	w
G2 H_2N	C7 H–C(1′)	w		C7 H_{eq}–C(5′)	w
	G8 H_{eq}–C(5′)	w	C7 H_2N^*	C7 H–C(5)	w
A3 H_2N	A4 H–C(8)	w		C7 H_2N^o	s
	C7 H_2N^o	w		G8 H–C(8)	w
	C7 H–C(5)	m	C7 H_2N^o	A3 H_2N	w
A4 H_2N	A4 H–C(2)	w		C7 H–C(5)	s
T5 HN	A4 H–C(2)	m		C7 H_2N^*	s
	A4 H_2N	m		G8 H–C(8)	w
	T5 H–C(1′)	w	G8 H_2N	C1 H–C(1′)	w
	T5 H–C(6)	w		G2 H_{ax}–C(5′)	w
	T5 H_3C–C(5)	w		G2 H_{eq}–C(5′)	w
	T6 H–C(1′)	w			
	T6 H_{ax}–C(5′)	w			
	T6 H_{eq}–C(5′)	w			

[a]) Cytidine -NH_2 protons are labeled with * for the H-bound proton, and with ^{o} for the not H-bound one.

The observation of sharp imino resonances and a set of only moderately broadened amino resonances at room temperature in a short duplex such as **1** is a clear sign of strong pairing. In comparison, only broad imino resonances and almost featureless amino signals, which did not give any NOESY cross peaks, were observed even at 4° in the earlier NMR study of the homo-DNA ddGlc-(AAAAATTTTT) duplex [6].

Current models of proton exchange in DNA duplexes presume that imino protons exchange in the opened state of the base pair [19]. That the imino proton of the first (and last) base pair is completely missing in the spectrum of **1**, therefore, points to a rapid opening and closing of these base pairs and, presumably, to increased conformational dynamics at the end of the duplex.

Broadening of the signals of the inherently less acidic amino protons is generally attributed to fast rotation around the exocyclic C–NH_2 bond, which is slower in cytidine than in guanine and adenine [20]. In fact, we observed separate signals for the two amino protons of C7 (second base pair) and possibly C1 (first base pair). On the other hand, only one signal was detected for each of the amino groups of G2, A3, and A4. This leaves two

possible interpretations of our data: either rotation is fast enough to give a single signal for both protons, or the observed signals correspond to the amino protons involved in a H-bond, while the others are broadened beyond detection by exchange with the solvent. In principle, integration should easily allow to decide between these possibilities. However, the non-uniform excitation in the WATERGATE experiment, the strong overlap of signals and a poor baseline force us to leave this question open.

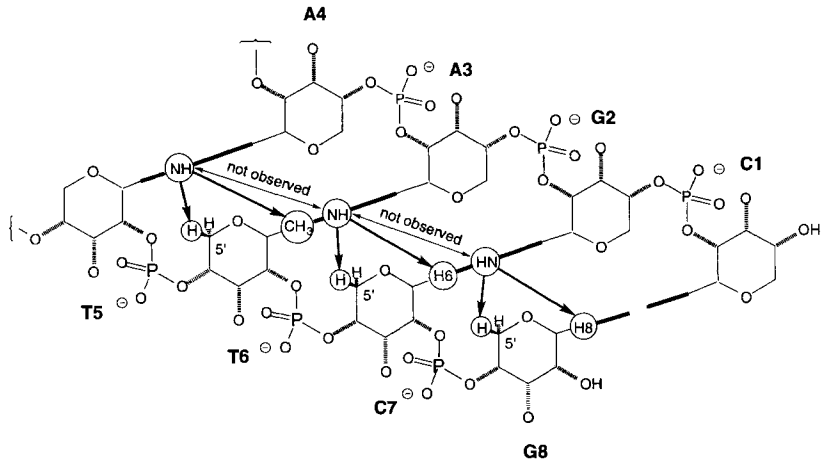

Fig. 11. *NOEs between exchangeable protons and protons of the adjacent nucleotide unit* (the corresponding NOEs to the strand drawn on top are omitted for clarity)

In regular double helical forms of natural DNA, imino protons of adjacent base pairs are stacked above each other near the main axis, and NOESY cross-peaks between them are regularly used for sequential assignments [9]. In contrast, no such cross-peaks were observed at all for **1**. Instead, a pattern of NOEs between imino protons and non-exchangeable protons on the aromatic rings (G8 H–C(8), C7 H–C(6), T6 Me) of the adjacent bases in both strands was observed (*Fig. 11*). Together with the NOEs between the amino protons of guanine and the H–C(1′) and H_{eq}–C(5′) protons of the next pyranose unit in the sequence, these correlations prove that adjacent base pairs must be offset against each other, consistent with an angle of 35° to 45° between the average axis of the base pairs and the backbone axis as derived above. Such a strong inclination puts neighboring bases belonging to opposite strands into a relative position well-suited for *inter*strand π-π stacking between either two purines, or a purine and a pyrimidine, but not between two pyrimidines (*Fig. 12*).

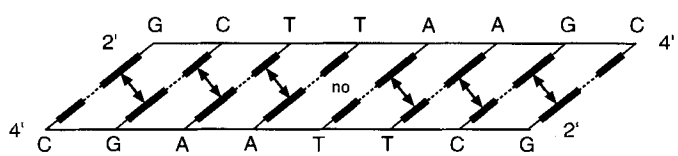

Fig. 12. *Interstrand stacking is possible between two purines, or a purine and a pyrimidine, but not between two pyrimidines*

3. Computer Simulations. – Molecular-dynamics (MD) calculations on the duplex **1** were carried out using the AMBER force field (for computational details, see *Exper. Part*). The starting structure was generated by duplication of a single strand in the idealized conformation (see *Fig. 1*). A duplex was formed by short MD sequences with intermittent minimizations, simultaneously enforcing the required *Watson-Crick* H-bonds at the initial stages of this process. Eventually, *all constraints were removed* to obtain a fully relaxed duplex structure. This geometry was used as a starting point for subsequent MD trajectories. All average structural parameters discussed below were calculated from a 1000 ps MD trajectory at 300 K from which instantaneous structures were recorded every 2 ps.

Observations on the Global Structure of the Duplex. The time evolution of the potential- and the kinetic-energy components during the simulation shown in *Fig. 13* reveals that no serious drifts or strong fluctuations occurred. While this may be taken as an indication that the system is equilibrated, symmetry considerations imply that all time-averaged values must tend to be equal in symmetry-related residues[8]). Although the system fails this control in the strict sense, the observed differences between the two strands are marginal enough to regard the system as basically equilibrated.

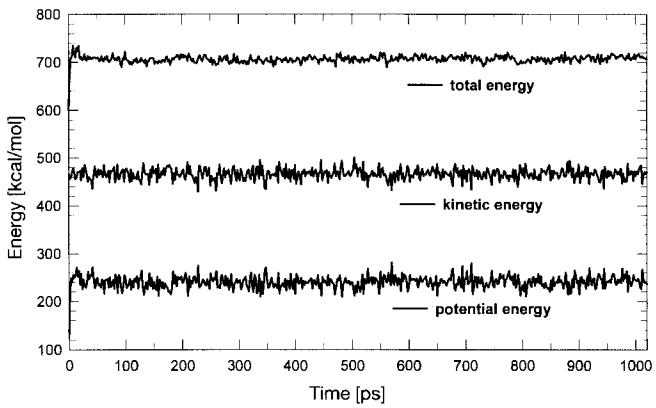

Fig. 13. *Time evolution of the potential, the kinetic, and the total energy during the MD simulation*

The average MD structure of the duplex has all *Watson-Crick* H-bonds for the six 'inner' residues conserved (see *Fig. 14*, left). The terminal residues fluctuate more strongly, and their time-averaged coordinates do not make sense graphically. The ten superimposed structures in *Fig. 14* (right), captured every 100 ps, illustrate the fluctuations during the MD trajectory, especially the stronger motion of the terminal residues C1, G8, C9, and G16. All pyranose rings stay in the starting low-energy chair conformation, as judged by only moderate fluctuations in γ and δ.

---

[8]) Since the NMR data exhibit full C_2 symmetry, the residues are labeled from C1 to G8 in the NMR part. For the computer simulations, where the two constitutionally equivalent residues are not necessarily symmetrical, labeling from C1 to G16 is used (*e.g.*, C1 [NMR] corresponds to C1 *and* C9 [MD]).

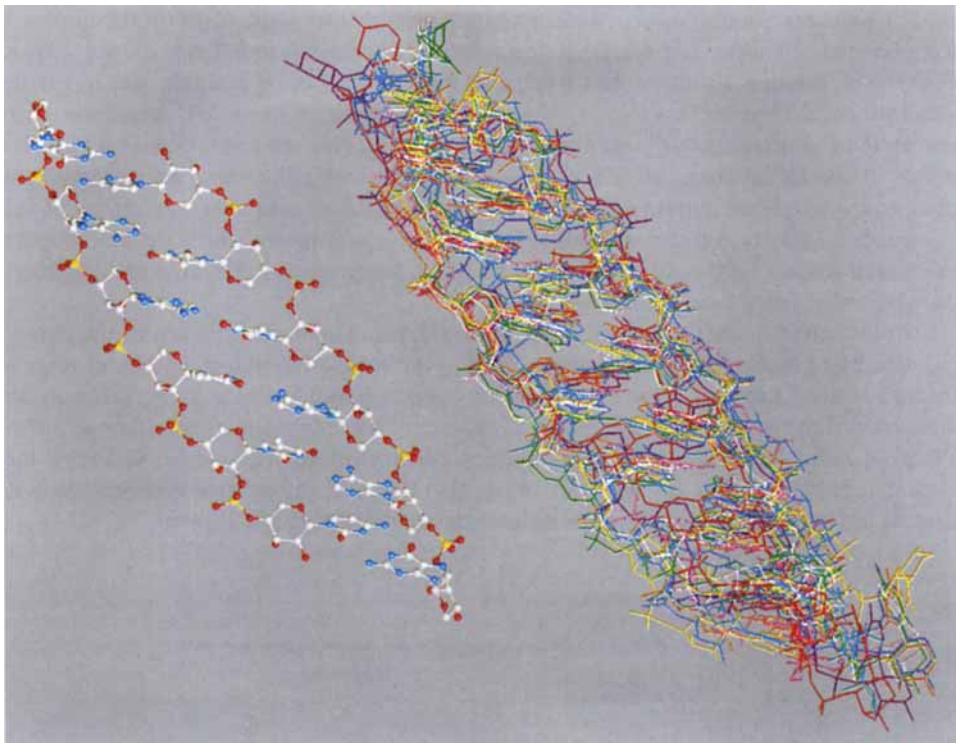

Fig. 14. *Time-averaged structure of the six inner residues of the octamer duplex* (left) *and superposition of ten structures equally spaced by 100 ps* (right). Hydrogens have been omitted for clarity.

The duplex is stabilized by two types of *inter*strand interactions, the *Watson-Crick* H-bonds (represented by the dotted lines in *Fig. 12*) as in standard DNA-DNA, DNA-RNA, or RNA-RNA double helices, and the *inter*strand stacking (shown schematically as arrows in *Fig. 12*), a characteristic of p-RNA which is thought to contribute to the experimentally observed high stability of the p-RNA duplex [3]. The octamer duplex analyzed here has two C–G pairs at each end, while the middle is constituted by four T–A pairs. In addition to the energetically less favorable H-bonding scheme of the T–A pair with respect to the C–G pair, the *inter*strand stacking is perturbed in the middle of the duplex, since the bases T5 (strand 1) and T13 (strand 2) cannot stack for geometrical reasons. *Figs. 15–17* show typical examples of purine-purine (*Fig. 15*) and purine-pyrimidine *inter*strand stacking (*Fig. 16*), and the impossibility to have optimal stacking for pyrimidine-pyrimidine, as occurring in the middle of the duplex (*Fig. 17*).

An idealized p-RNA duplex with all bond angles along the backbone perfectly tetrahedral and the phosphodiester linkage conformation $\varepsilon = -60°$; $\zeta = 180°$, $\alpha = 60°$, $\beta = 180°$ would assume a *quasi*-linear 'inclined ladder-like' structure. The deviations from this idealized conformation in the calculated average structure lead to a left-handed helix which is more pronounced in a fully energy-minimized structure but never vanishes during the course of the MD trajectory, and is clearly apparent in the MD average geometry. The helix has a periodicity of *ca.* 18 to 19 monomers per turn and a pitch of *ca.* 110 Å.

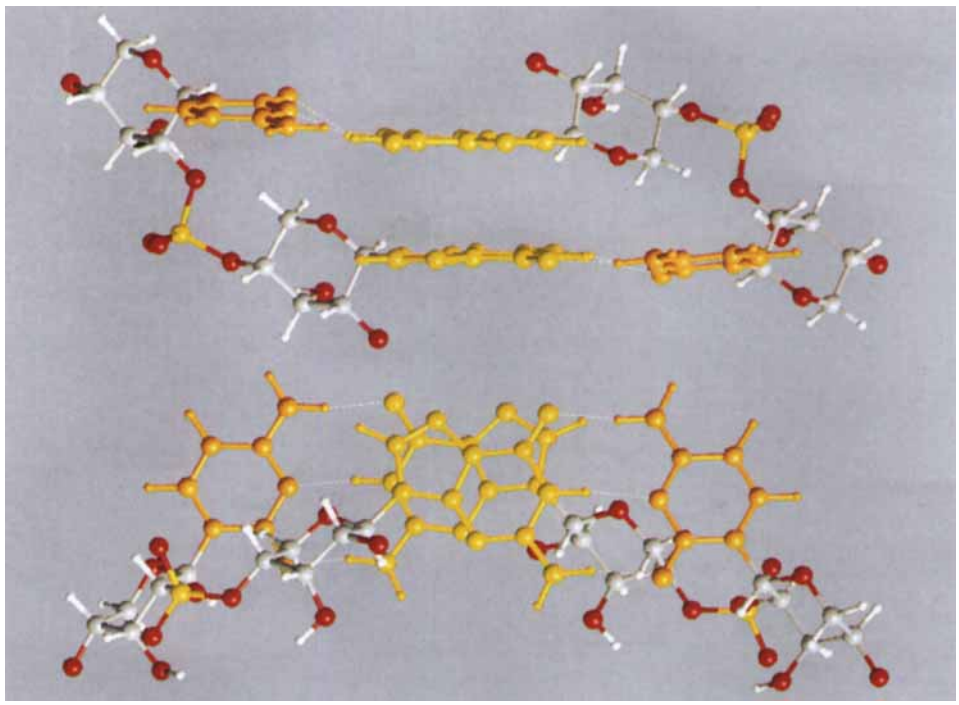

Fig. 15. *Purine-purine* (G16-G2 or G10-G8) *interstrand stacking* (side and bottom view)

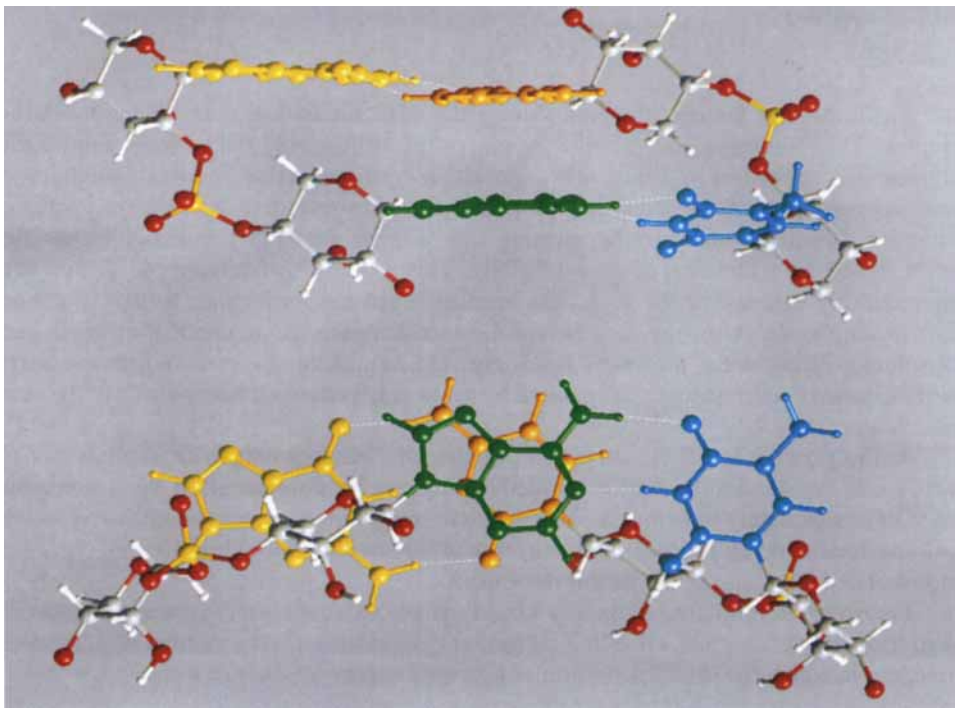

Fig. 16. *Pyrimidine-purine* (C15-A3) *interstrand stacking* (side and bottom view)

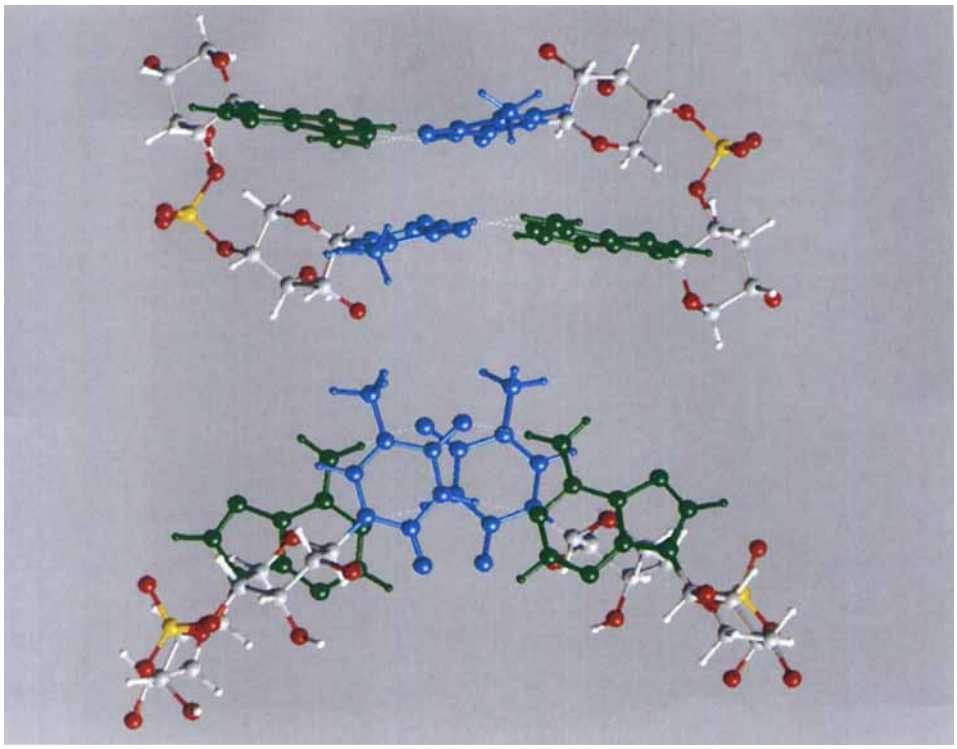

Fig. 17. *Lack of pyrimidine-pyrimidine* (T13-T5) *interstrand stacking* (side and bottom view)

An interesting feature observed during the MD simulation is the bending of the duplex. This motion is only possible in one direction, towards the concave side of the duplex (see definition in *Footnote 6*). Resulting from concerted moderate changes in various torsional angles, it cannot be traced down to one or a few abrupt localized changes. It can be analyzed by plotting the distance between terminal P-atoms for each strand as a function of time (*Fig. 18*). This span is normally *ca.* 40 Å and can momentarily decrease below 30 Å. The bending is not strictly regular, neither in period nor in amplitude. Also, the momentary distance between the terminal P-atoms is not absolutely identical for the two strands (see *Fig. 18*), although its variation is always simultaneous in both strands, as required by the largely conserved base pairing in the bent geometry.

At this point, it is difficult to decide whether this bending is real, or whether it is an artifact of the simulation. However, the bending can be reproduced on rigid molecular models in which only torsional angles are free to rotate, whereas bond lengths and angles are confined to default values. Its occurrence in the simulation is a hint that no repulsive non-bonded interactions forbid this movement.

The observed frequency of *ca.* 3 to 4 bendings per ns would imply an energy barrier of 4 to 5 kcal · mol^{-1}, a small value in a molecular system with a large number of degrees of freedom in which the total fluctuation of potential energy is much larger.

The most extreme bending (corresponding to the peak at *ca.* 240 ps in *Fig. 18*) is visualized in *Fig. 19*, together with a fully extended p-RNA duplex.

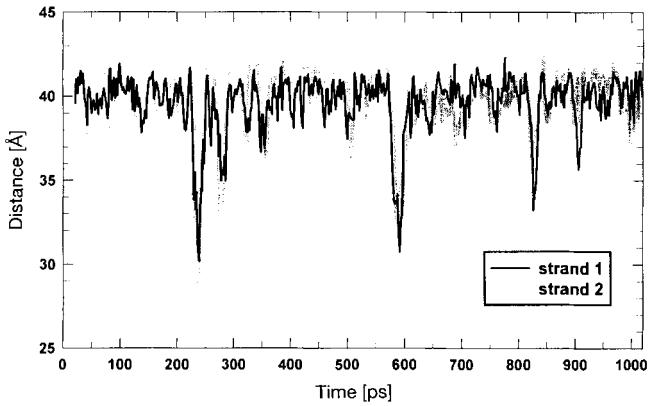

Fig. 18. *Distance between the terminal P-atoms in strand 1 and in strand 2 as a function of time, indicating strong duplex bending at various stages of the MD trajectory*

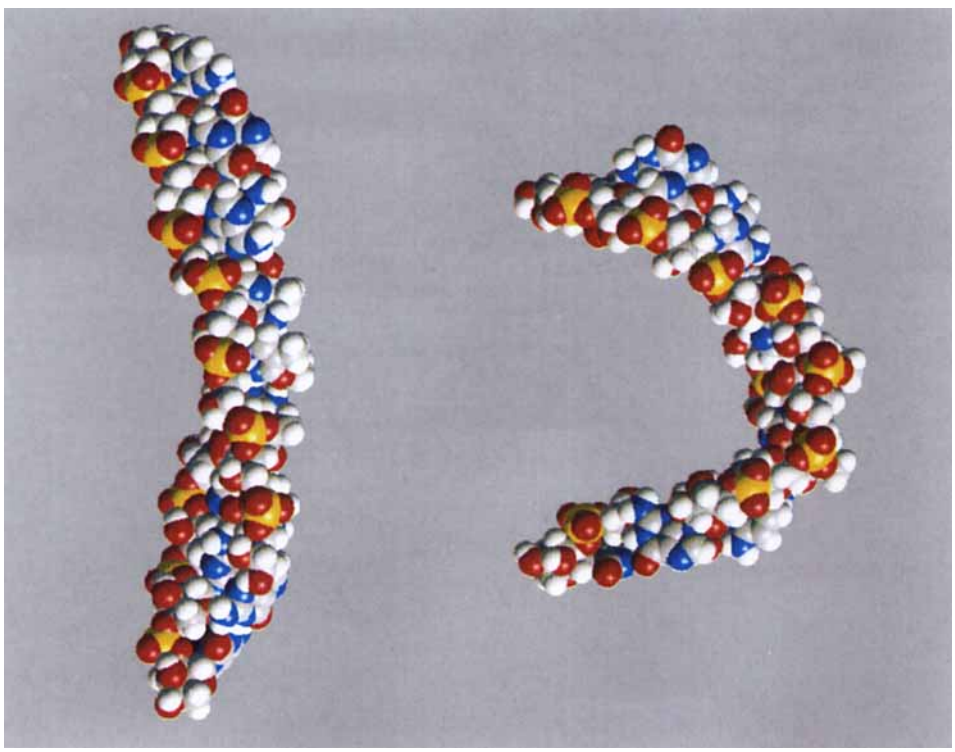

Fig. 19. *Fully extended* (left) *and strongly bent* (right) *duplex, corresponding to maximum and minimum for the P–P distance shown in* Fig. 18

Structural Details. A full analysis of the MD averages for torsional angles around freely rotating bonds is compiled in *Fig. 20.* The endocyclic torsional angles γ and δ have been omitted from a detailed analysis once it was verified that the pyranose rings oscillate around the initial chair conformation. Except in the phosphodiester linkages towards the terminal residues, all respective torsional angles are quite similar in all residues. A definite sequence dependency cannot be detected: α ranges between 72° and 77° (±12° to 20°); β assumes values in the range from 156° to 169° (±14° to 23°), ε and ζ are both confined to a narrower range with $\varepsilon = -80°$ to $-83°$ (±13° to 15°), and $\zeta = -174°$ to $-177°$ (±11° to 13°). Thus, the conformation type of the phosphodiester linkage between two residues $\{\varepsilon; \zeta; \alpha; \beta\}$ can be described as $(g^-; t; g^+; t)$. The glycosidic torsional angle χ fluctuates between 123° and 133°.

The time evolution of selected backbone torsional angles is shown as polar plots in *Fig. 21.* Except for terminal residues, the time evolution in all residues is quite stable and similar. Definite conformational transitions are rare and very short, *e.g.*, α in residue A4.

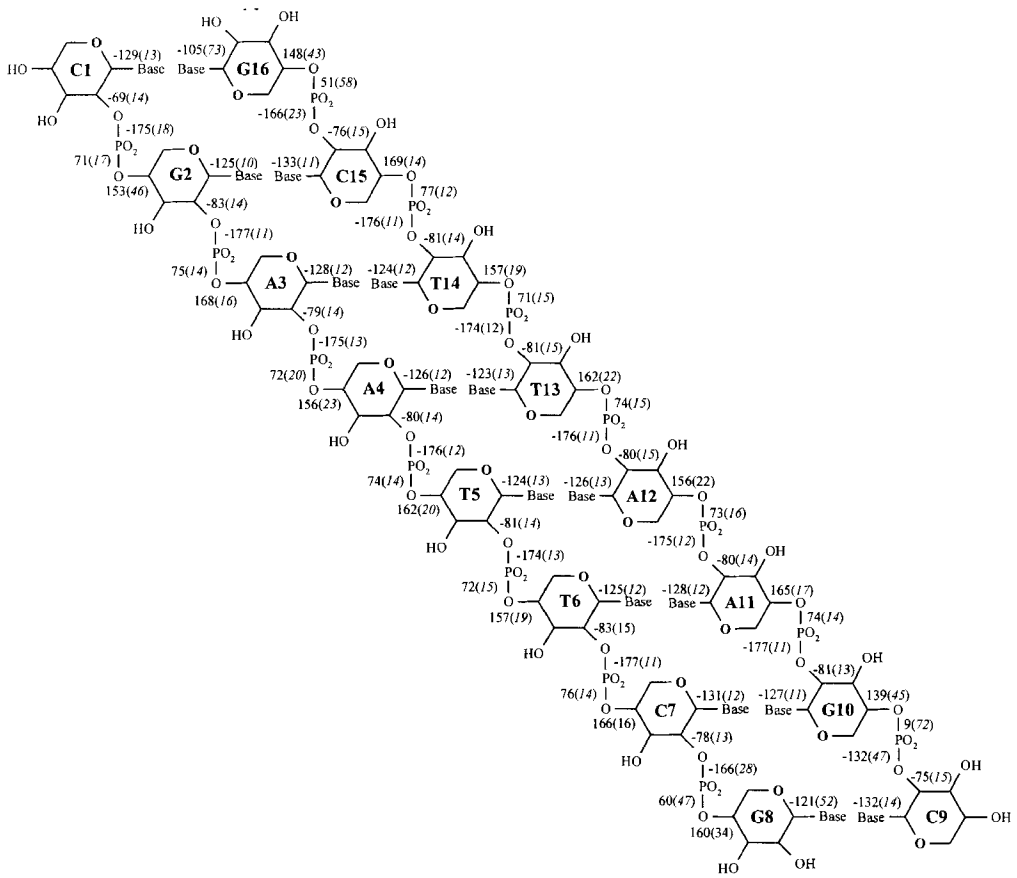

Fig. 20. *Torsional angles averaged over the 1000 ps MD trajectory with standard deviations in parentheses.* Data compiled from 500 individual instantaneous structures (spaced by 2 picoseconds).

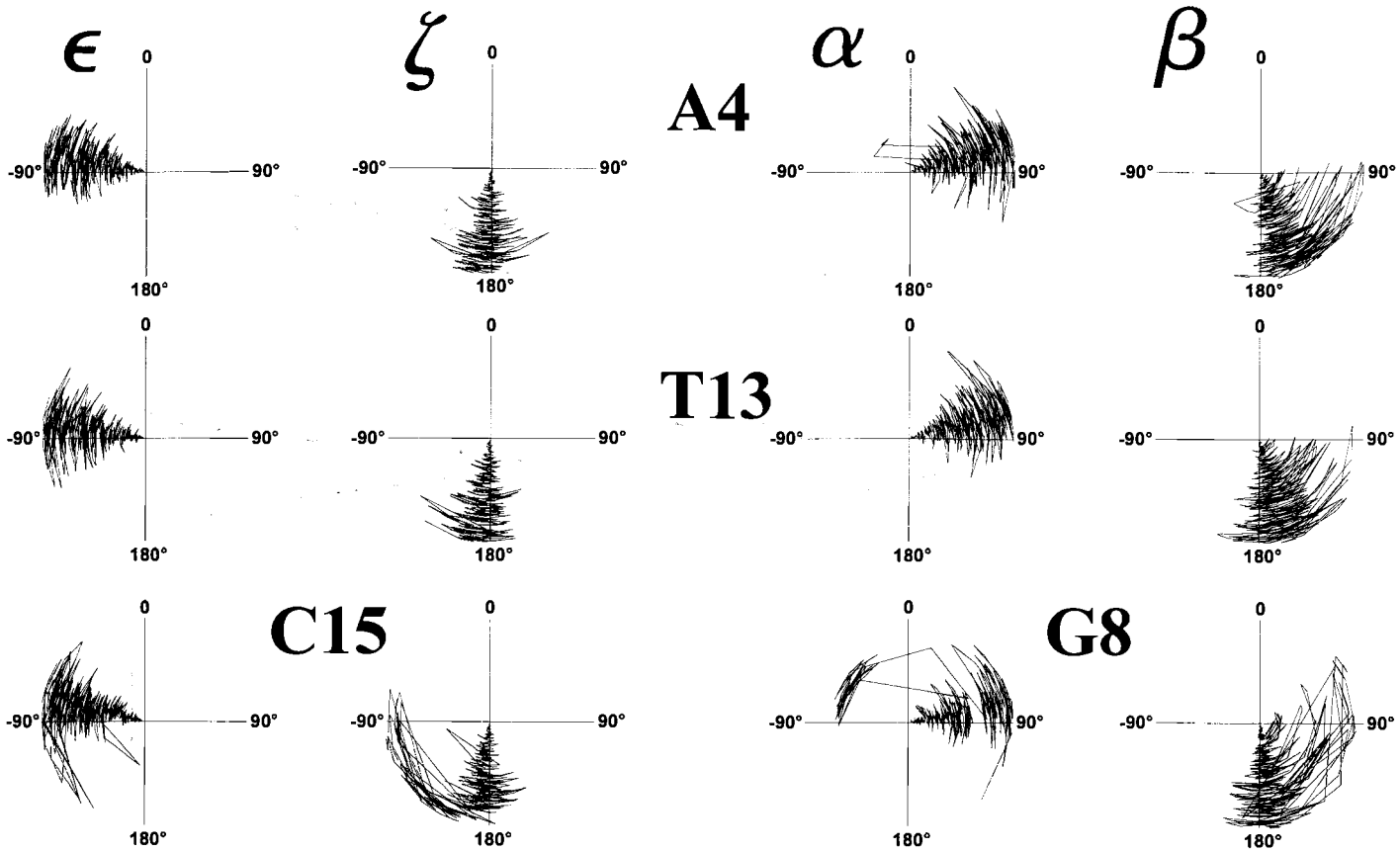

Fig. 21. *Polar plots for the time evolution of torsion angles ε, ζ, α, and β in selected phosphodiester linkages.* The phase corresponds to the actual angle, the radial coordinate is the time axis, going from 0 to 1 ns. Residues A4 and T13 are typical for all inner residues. ε and ζ in C15, and α and β in G8 display the stronger fluctuations in terminal residues (note that the very nature of polar plots leads to a visual increase of the scattering with increasing radius).

That the terminal residues are moving quite freely is apparent from the strong fluctuations of α and β in G2, G8, G10, G16, and of ζ in residues G8, G10, and G16. The lack of symmetry in the average motion of the terminal residues is an obvious indication that the system was not equilibrated with regard to these highly chaotic transitions.

Fig. 21 reveals qualitatively that α and β fluctuate more strongly than ε and ζ. Especially β seems to oscillate with a higher amplitude. The distribution of β was evaluated in detail for all 14 residues in which it occurs. The distribution functions, compiled from the 500 individually saved MD structures, are depicted in *Fig. 22*. Note again that in both strands the corresponding functions are similar, although not strictly identical as would be required by symmetry. The curves reveal that the major population

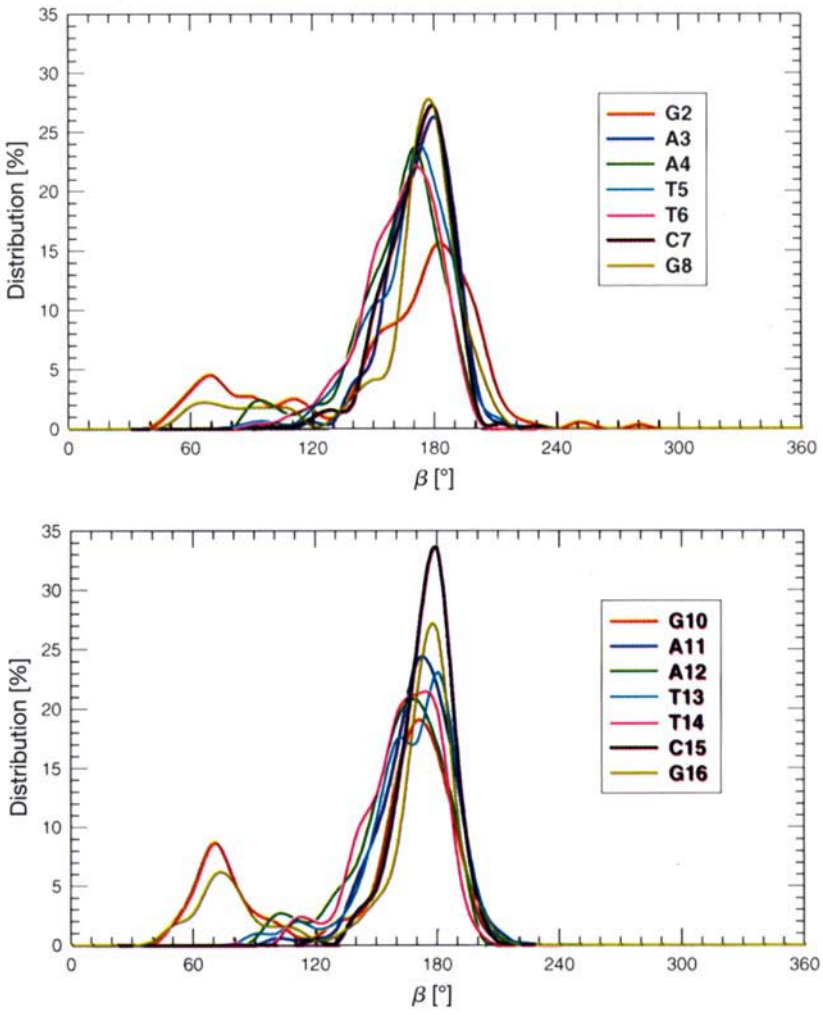

Fig. 22. *Distribution of β in all residues of strand 1* (top) *and strand 2* (bottom), *compiled from 500 equally spaced instantaneous structures captured during the 1 ns MD trajectory*

of β is around 160–170°, with a tail (and sometimes a shoulder) towards smaller values. Also, the terminal residues have a significant population around 70°, *i.e.*, in the g^+ domain, illustrating the conformational disorder at the ends of the duplex.

Comparison with Experiment. For comparison with the experimental values, time-averaged coupling constants were calculated from the 500 recorded structures of the MD trajectory by application of the *Karplus* relations [10]

$$^3J(\text{HCOP}) = 15.3\cos^2\varphi - 6.2\cos\varphi + 1.5 \quad (1)$$

$$^3J(\text{CCOP}) = 8.0\cos^2\varphi - 3.4\cos\varphi + 0.5 \quad (2)$$

on the torsional angles φ = H(4′)–C(4′)–O(4′)–P and φ = H(2′)–C(2′)–O(2′)–P for H,P coupling, and φ = C(5′)–C(4′)–O(4′)–P, φ = C(1′)–C(2′)–O(2′)–P, φ = C(3′)–C(4′)–O(4′)–P, and φ = C(3′)–C(2′)–O(2′)–P for C,P coupling. Experimental and simulated data are compiled in *Table 6*.

Table 6. *Calculated* (MD) *and Experimental* (NMR) *Coupling Constants Defining the Torsion Angles β and ε of the Backbone*[a])

	Residue	^3J(4′,P(4′))	^3J(C(5′),P(4′))	^3J(C(3′),P(4′))	^3J(2′,P(2′))	^3J(C(1′),P(2′))	^3J(C(3′),P(2′))
MD	4′–C1				4.1 (2.4)	11.0 (1.2)	0.7 (0.6)
MD	4′–C9				4.9 (2.3)	10.7 (1.2)	0.6 (0.8)
NMR	C1				7.2 (0.5)	11 (0.5)	n.d.
MD	G2	4.2 (3.1)	3.1 (3.9)	8.5 (4.3)	6.1 (2.4)	9.9 (1.7)	0.6 (0.7)
MD	G10	4.3 (2.6)	3.5 (4.6)	8.0 (4.6)	5.8 (2.3)	10.1 (1.5)	0.6 (0.6)
NMR	G2	10 (1)	3.1 (0.5)	n.d.	6.9 (0.5)	11 (0.5)	n.d.
MD	A3	4.1 (2.5)	0.8 (0.9)	10.8 (1.6)	5.6 (2.4)	10.2 (1.7)	0.6 (0.6)
MD	A11	4.6 (2.7)	0.9 (1.0)	10.6 (1.8)	5.7 (2.4)	10.2 (1.6)	0.6 (0.7)
NMR	A3	n.d.	3.1 (0.5)	n.d.	7.4 (0.5)	11 (0.5)	n.d.
MD	A4	5.5 (2.8)	1.2 (2.0)	9.6 (2.9)	5.7 (2.4)	10.2 (1.6)	0.6 (0.6)
MD	A12	5.6 (2.9)	1.3 (1.9)	9.5 (2.9)	5.6 (2.4)	10.1 (1.7)	0.6 (0.7)
NMR	A4	n.d.	3.1 (0.5)	8 (1)	7.8 (0.5)	11 (0.5)	< 1.5
MD	T5	5.0 (2.9)	1.0 (1.4)	10.2 (2.3)	6.1 (2.5)	9.9 (1.7)	0.6 (0.7)
MD	T13	4.8 (2.8)	1.2 (1.7)	10.1 (2.6)	6.1 (2.5)	9.9 (1.8)	0.7 (0.8)
NMR	T5	10 (1)	n.d.	n.d.	7.1 (0.5)	11.2 (0.5)	n.d.
MD	T6	5.5 (2.8)	1.0 (1.4)	9.8 (2.4)	6.2 (2.5)	9.8 (1.9)	0.7 (0.9)
MD	T14	5.6 (2.8)	1.0 (1.4)	9.8 (2.5)	6.1 (2.4)	10.0 (1.7)	0.6 (0.7)
NMR	T6	9 (1)	n.d.	8 (1)	7.4 (0.5)	9.5 (0.5)	< 1.5
MD	C7	4.4 (2.6)	0.8 (0.9)	10.7 (1.7)	5.3 (2.3)	10.5 (1.5)	0.5 (0.7)
MD	C15	3.8 (2.3)	0.7 (0.7)	11.1 (1.2)	5.1 (2.3)	10.5 (1.6)	0.6 (1.0)
NMR	C7	9 (1)	n.d.	8 (1)	8.3 (0.5)	9.5 (0.5)	< 1.5
MD	G8-2′	3.7 (2.4)	2.0 (3.2)	9.9 (3.5)			
MD	G16-2′	3.9 (2.3)	2.9 (4.3)	8.8 (4.4)			
NMR	G8	10.5 (1)	n.d.	n.d.			

[a]) The simulation results refer to individual residues and are averaged over 500 individual instantaneous MD structures. Note that the experimental data cannot differentiate between the symmetry-related residues. The values in parentheses are standard deviations in the case of simulated data and estimated errors in the case of experimental data, n.d.: not determined.

For ε, the agreement between simulation and experiment is excellent. No resolved coupling was observed for ^3J(P(2′),C(3′)) which corresponds to ε itself. This is consistent with the simulation which predicts a very low coupling constant (< 1 Hz).

For β, the agreement between computed and measured coupling constants is not satisfactory. Because the slope of the *Karplus* functions for ^3J(C,P) and ^3J(H,P) is different for the three regions of interest here, the discrepancy between calculated and measured coupling constants is largest for ^3J(4′,P(4′)) and smaller for the two ^3J(C,P) values. However, comparison of dihedral angles instead of coupling constants (see *Fig. 23*) reveals that the complementary dihedral angles φ determined from experimental coupling constants (horizontal bars at the top of the diagram) deviate systematically by *ca.* 25° from the corresponding angles predicted by the MD calculations (distributions represented by vertical bars). Assuming that the used *Karplus* parameters are valid, as corroborated by the test with cyclophosphates **2–4** (see *Exper. Part*), the reasons for the disagreement must be looked for elsewhere. A possible source for the disagreement might be related to inadequate force-field parameters. While AMBER performs well for natural nucleic acids with furanose sugars, the global parametrization might have deficiencies for the pyranose sugars in this case.

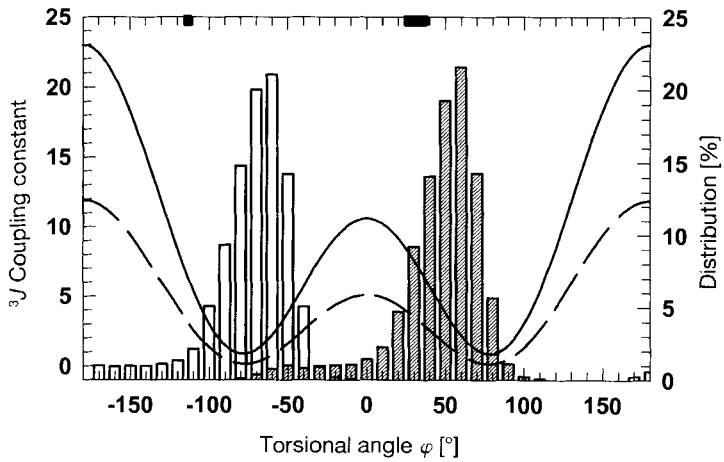

Fig. 23. Karplus *functions for* $^3J(H,P)$ (solid line) *and* $^3J(C,P)$ (dashed line), *according to* Eqns. 1 *and* 2 [10]. The bars represent the distribution of φ = H4′–C4′–O4′–P and φ = C5′–C4′–O4′–P, respectively. The distributions include all residues except the terminal ones, taken over the entire MD simulation, at 2 ps intervals (*i.e.*, 6000 data points for each distribution). The solid bars at the upper x-axis represent the range of experimental φ values (taken over all residues, including the experimental error).

Another source of discrepancy could be the admittedly crude treatment of the electrostatic interactions using a distance-dependent dielectric function instead of explicit water. However, the attempts to include explicit solvent and counterions described in the section about computational methods (see *Exper. Part*) did not result in a better agreement for β while introducing new discrepancies for ε. The goal of the explicit solvent simulation was to detect possible strong interactions with individual H_2O molecules inducing a distinct solvation scheme. Nothing of that kind was observed during the 500-ps simulation. However, because of the higher viscosity of the system with explicit H_2O, some conformational changes involving mainly ε and ζ, which occurred at the initial stages of the simulation, did not recover to experimentally observed values during this obviously too

short simulation. A longer simulation with explicit solvent and periodic boundary conditions including the complete octamer without any artificial constraints might be envisaged. At this point, however, we have no indication that the results would be in better agreement with the experimental data. On the other hand, features like the bending of the duplex might not be observed in a simulation in which all transitions are slowed down by friction with H_2O molecules.

4. Conclusion. – The self consistency of the structural parameters derived from the NMR data, together with the reasonable average structure calculated from the MD trajectory for the six inner residues, indicate that a single conformation type of the p-RNA duplex dominates in solution, and that no other backbone conformations are low enough in energy to have important statistical-mechanical weights.

Both, the NMR-derived conformational model and the average MD structure confirm the main structural features predicted by qualitative conformational analysis. The duplex displays *Watson-Crick* pairing with antiparallel strand orientation. The strong inclination of the average base-pair axis towards the backbone axis (*ca.* 40°) allows *inter*strand purine-purine and purine-pyrimidine stacking between neighboring base pairs. The preferred backbone conformation within the phosphodiester linkage can be characterized as $\{g^-; t; g^+; t\}$ in the sequence $\{\varepsilon; \zeta; \alpha; \beta\}$, and the pyranose rings assume a chair conformation with little deformation.

The experimentally derived torsional angles β and ε deviate considerably from the idealized values. Model considerations indicate that adjustment of these dihedral angles to the values found by NMR leads to better *inter*strand stacking and reduces the unfavorable 1–5 interaction between pyranose H- and O-atoms of the phosphodiester linkage. The MD simulation predicts average values for ε that agree well with the NMR-derived angle, whereas for β, the average MD structure deviates *ca.* 25° less from the idealized conformation than the NMR-consistent model. Therefore, the possibility that the AMBER foce field used here may underestimate certain interactions that are characteristic for p-RNA but not for natural DNA and RNA, especially *inter*strand π-π stacking, must be considered in future work on p-RNA structures.

While this study confirms that the fully paired p-RNA duplex **1** has a relatively rigid, quasi-linear structure, the interesting overall bending motion occurring in the MD trajectory and the conformational dynamics of terminal residues, found by both NMR and MD, indicate that p-RNA single strands may be flexible enough to assume different backbone conformations and, therefore, other tertiary structures, if the base sequence does not allow regular antiparallel pairing.

This work was supported by *Ciba-Geigy AG*, Basel, *Firmenich & Co.*, Geneva, and the *Schulleitung of the ETH-Zürich*. *I.S.* and *B.J.* thank Prof. *R. Ernst* for access to the 600-MHz NMR spectrometer, and Prof. *M. Dobler* for help with his molecular-modeling software.

Experimental Part

1. *Synthesis of* β-D-*Ribopyranosyl-(2′→4′)-(CGAATTCG)*[9]. The synthesis was carried out in two batches (20-μM scale each) on a *Pharmacia Gene Assembler Plus* following the procedure described in [2] but without

[9]) The synthesis of the phosphoramidite building blocks and of p-RNA oligonucleotide sequences will be reported in detail in this journal [21].

cleaving the last dimethoxytrityl group ('trityl on'). After Pd-assisted removal of the allyl protecting groups [22] and treatment with 25% aq. hydrazine for 20 h at 0°, the mixture was subjected to chromatography on reverse-phase *C-18* silica gel (elution with a H_2O/MeCN gradient). The isolated compound was treated with 80% aq. HCOOH for 20 min at ambient temp., and subsequently subjected to prep. HPLC (*Spherisorb* 300 Å, *C-18*, 10 μm, 250 × 9 mm; flow rate 4 ml/min; buffer *A*: 0.1M NH_4HCO_3 (pH 7.0) in H_2O, buffer *B*: 0.1M NH_4HCO_3 (pH 7.0) in H_2O/MeCN 1:4). After evaporation and lyophilization of the pooled fractions, 6.4 mg and 5.4 mg, resp., of a fluffy colorless powder were obtained. The material was chromatographically homogeneous and exhibited the correct mass in a MALDI-TOF mass spectrum[10]). From temp.-dependent UV spectra at various concentrations [23–25], the thermodynamic properties of duplex formation (0.15M NaCl, pH 7) were determined: $\Delta G_{298} = -12.55$ kcal mol^{-1}, $\Delta H^\circ = -54.89$ kcal mol^{-1}, $T\Delta S_{298} = -42.34$ kcal mol^{-1}K^{-1}. The transition temp. at $c = 10$ μM was 60° (sigmoidal melting curve, hyperchromicity 20% at 259 nm).

2. *NMR Spectroscopy. NMR Spectroscopy of* **1** *in* D_2O. *Sample Preparation. Sample A*: 6.4 mg of pr-(CGAATTCG) (as hydrated NH_4^+ salt) was lyophilized two times, the first time from H_2O, the second time from D_2O. The residue was dissolved in 0.4 ml of 0.05M sodium arsenate buffer in D_2O (obtained by lyophilization of 0.2 ml of 0.2M sodium arsenate buffer, pH 7.4 (*Sigma*) from D_2O).

Sample B: 5.3 mg of pr-(CGAATTCG) was added to *Sample A*. This sample also contained some Et_3NH^+ as counterion.

For all spectra (except ^{13}C with broad-band decoupling): *Bruker AMX 500* spectrometer at 11.7-T field strength, temp. 300 K. *For* ^{13}C *with broad-band decoupling: Bruker AMX 600* spectrometer at 14.1-T field strength.

1D Spectra. ^1H: 88-K data points acquired, 256 scans, no dummy scans, spectral width 8064.52 Hz; transformed to 64-K data points, polynomial base-line correction. ^{13}C: 32-K data points acquired, 114250 scans, 16 dummy scans, CPD decoupling using WALTZ-16 sequence, NOE presaturation; transformed to 128-K data points using a *Gauss* filter (LB –0.15 Hz, GB 0.045), polynomial base-line correction.

2D Spectra. COSY: DQF-COSY with modified phase cycle [26]; 4096 (ω_2) × 448 (ω_1) data points acquired, 64 scans per FID, 16 dummy scans, 5050.5-Hz spectral width in both dimensions, phase-sensitive (TPPI); transformed after multiplication with a sine square filter shifted by $\pi/2$ in ω_1 and ω_2 to give a 4 K × 4 K data matrix. *COSY with* $\{^{31}P\}$ *decoupling during* t_2: DQF-COSY with modified phase cycle [26] and $\{^{31}P\}$-CPD decoupling using WALTZ-16 during t_2; other parameters identical to the COSY spectras without ^{31}P-decoupling.

TOCSY: with DIPSI-2 and *z*-filter [27]; 2048 (ω_2) × 512 (ω_1) data points acquired, 32 scans per FID, 16 dummy scans, 5050.5-Hz spectral width in both dimensions, phase-sensitive (TPPI), mixing time 80 ms, B_2 field strength 10 kHz; transformed after multiplication with a sine square filter shifted by $\pi/2$ in ω_2 and $\pi/3$ in ω_1 to give a 2 K × 2 K data matrix, polynomial base-line correction in both dimensions.

ROESY: with 90° trim pulses before and after spin lock period [28]; 2048 (ω_2) × 632 (ω_1) data points acquired, 48 scans per FID, 32 dummy scans, 4587.16-Hz spectral width in both dimensions, phase-sensitive (TPPI), 150 ms mixing time, CW spin lock with $\gamma B_2/2\pi = 3$ kHz; transformed after multiplication with a sine square filter shifted by $\pi/2$ in ω_2 and in ω_1 to give a 2 K × 2 K data matrix, polynomial base line correction in both dimensions.

NOESY: phase-sensitive [29] with 40, 60, 80, or 150 ms mixing time; 4096 (ω_2) × 840 (ω_1) data points acquired, 48 scans per FID, 32 dummy scans, 4716.98-Hz spectral width in both dimensions, phase-sensitive (TPPI); transformed after multiplication with a sine square filter shifted by $\pi/2$ in ω_2 and ω_1 to give a 2 K × 2 K data matrix, polynomial base-line correction in both dimensions.

[^1H,^{31}P*]-COSY*: ^1H detected [30] 2048 (ω_2) × 256 (ω_1) data points acquired, 64 scans per FID, 16 dummy scans, 5050.5-Hz spectral width in ω_2, 1014.2 Hz spectral width in ω_1, phase-sensitive (TPPI); transformed after multiplication with a sine square filter shifted by $\pi/2$ in ω_2 and ω_1 to give a 2 K × 2 K data matrix, polynomial base-line correction in both dimensions.

HSQC: [^1H,^{13}C]-HSQC with gradients for coherence selection [31]; 4096 (ω_2) × 512 (ω_1) data points acquired, 224 scans per FID, 32 dummy scans, phase-sensitive (TPPI), GARP ^{13}C decoupling during t_2, 4504.5 Hz (ω_2) × 23809 Hz (ω_1) spectral width; transformed after multiplication with a sine square filter shifted by $\pi/2$ in ω_2 and ω_1 to give a 2 K × 2 K data matrix.

NMR Spectroscopy of **1** *in* H_2O/D_2O *9:1. Sample Preparation. Sample A* was lyophilized once and then dissolved in 0.4 ml of H_2O/D_2O 9:1. *For all spectra: Bruker AMX 500* spectrometer at 11.7-T field strength, temp. 300 K.

---

[10]) We thank Dr. *U. Piels* and Dr. *H. Moser* (*Ciba AG*, Basel) for determination of the MALDI-TOF spectra in their laboratory.

1D Spectra. ^1H: 32-K data points acquired, 256 scans, 4 dummy scans, spectral width 10204.08 Hz, water suppression using WATERGATE pulse sequence [32]; transformed to 32-K data points, polynomial base line correction.

2D Spectra. NOESY (high digital resolution): 150-ms mixing time; 4096 (ω_2) × 1024 (ω_1) data points acquired, 64 scans per FID, 4 dummy scans, phase sensitive (TPPI), water suppression using WATERGATE [33], 10204.8-Hz spectral width in both dimensions; transformed after multiplication with a sine square filter shifted by $\pi/2$ in ω_2 and ω_1 to give a 2 K × 2 K data matrix, polynomial base line correction in both dimensions.

NOESY (lower digital resolution): 80- or 150-ms mixing time; 4096 (ω_2) × 420 (ω_1) data points acquired, other parameters as above; transformed after multiplication with a sine square filter shifted by $\pi/2$ in ω_2 and $\pi/3$ in ω_1 to give a 2 K × 2 K data matrix, polynomial base line correction in both dimensions.

Determination of Coupling Constants. ^3J(P,C): Coupling constants were determined by fitting of a sum of two *Lorentz* curves (using the program MATLAB) to the peaks in the broad-band-decoupled ^{13}C spectrum. Strong overlap of signals in the region of C(3′), C(4′), and C(5′) as well as a low signal-to-noise ratio made it impossible to determine all coupling constants. ^3J(P,H): These coupling constants were extracted from COSY spectra by comparing corresponding traces of the $\{^{31}P\}$-decoupled (during t_2) and not $\{^{31}P\}$-decoupled COSY spectra. For J(2′,P), 2 respectively 4 *Gauss* lines had to be fitted to the traces; for J(4′,P) 8 resp. 16 lines due to the additional coupling between H_{eq}–C(5′), H_{ax}–C(5′), and H–C(4′). ^3J(H,H): As a by-product from the determination of ^3J(P,H) one also obtained ^3J(H,H) coupling constants.

Calibration of Karplus *Relations.* The ^1H- and ^{13}C-NMR spectra of compounds **2**–**4**[11]) were measured, fully assigned and the corresponding ^3J(C,P) and ^3J(H,P) constants determined.

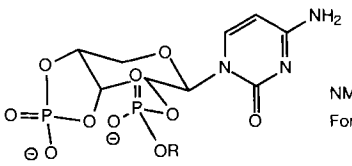

2

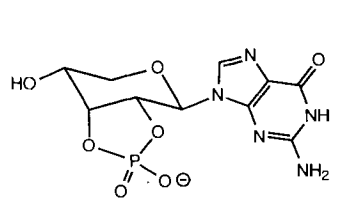

3

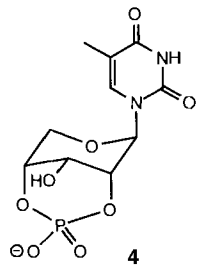

4

Although it could be expected that the bicyclic nature of **2**–**4** would lead to single, dominant conformations, this assumption was tested by subjecting the three structures to force-field calculations. For each structure, 100 conformations were generated by 'rapid quenching' followed by energy minimization of all non-identical conformations. For each of the resulting conformers, the coupling constants were calculated from dihedral angles and the *Karplus* equation to be tested. Finally, the theoretical J values were averaged, whereby each conformer was weighted according to its minimized energy (artificial '*Boltzmann* distribution').

3. *Molecular-Dynamics Calculations. Computational Methods and Definitions.* All computations have been carried out with the AMBER [34] force field as incorporated in the software package *InsightII(2.3)/Discover(2.9.7)* of *MSI*, San Diego, CA, USA. Only original AMBER parameters were used, and no additional potential atom types were defined. The partial charges used in the electrostatic (*Coulomb*) term were attributed by a donor-acceptor scheme which closely fits the original AMBER partial charges in those structural entities found in standard DNA or RNA.

---

[11]) S. Pitsch, G. Hanquet, ETH-Zurich, unpublished work.

Calculations were performed on *Crimson* and *Power Challenge* workstations from *Silicon Graphics*, Mountain View, Ca, USA.

The simulations were carried out for the octamer duplex **1**. The initial structure was built by generating a single strand octamer in the idealized conformation throughout the backbone, *i.e.*, $\varepsilon = -60°, \zeta = 180°, \alpha = 60°, \beta = 180°$, the sugar six-ring assuming a standard chair conformation. The torsional angles are defined like in DNA or RNA, following the *IUPAC* nomenclature for nucleic acids (see *Fig. 1*).

The single-strand octamer built with an idealized geometry was duplicated, yielding a pair of self-complementary stands. A duplex was formed by short MD sequences with intermittent minimizations, simultaneously enforcing the required *Watson-Crick* H-bonds at the initial stages of this process. Eventually all constraints were removed to obtain a fully relaxed duplex structure. This geometry was used as a starting point for subsequent MD trajectories.

Various MD simulations were carried out under different conditions. All results reported below were eventually obtained by neglecting explicit counterions (solvated or not) and H_2O. A distance-dependent permittivity $\varepsilon = 4r$ was used to simulate an aq. environment. No artificial constraints were applied to the system, *i.e.*, all atoms were free to move within the natural constraints imposed by the bonded and nonbonded interactions of the force field. Also, no cutoff distance was applied for nonbonded interactions. The system was equilibrated by progressive heating to 300 K: 1 ps at 50 K and 100 K, 2 ps at 150 K, 3 ps at 200 K, 8 ps at 250 K, and 20 ps at 300 K. The production trajectory was run for 1 ns at 300 K. The temp. was held constant by coupling to an external heat bath [35]. One-femto-second time steps were used in the numerical integration of the equations of motion. Instantaneous structures (to be used for further analysis) were recorded at 2-ps intervals, *i.e.*, all reported average values were obtained from 500 individual geometries.

A test simulation with hydrated Na^+ counterions, using the settings and parameters as described by *Singh et al.* [36] revealed that the presence of these charge-compensating entities does not influence the data of interest here, *i.e.*, mainly geometrical factors. This is in accordance with the observations of *Singh et al.* for a short B-DNA duplex [36]. Furthermore, a 500-ps simulation with explicit counterions and H_2O molecules ($\varepsilon = 1$) was performed on the central part of the duplex, including A3 to T6 and A11 to T14. All atoms in residues A3, T6, A11, and T14 were fixed during the entire simulation, and only the four residues A4, T5, A12, and A13 were allowed to move freely under the constraints imposed by the force field. The system was surrounded by a sphere of 20-Å diameter of randomly oriented TIP3P [37] H_2O molecules at a density of 1 $g \cdot ml^{-3}$. The water was kept from 'evaporating' by applying a harmonic repelling potential on the O-atoms of H_2O molecules trying to escape the sphere. The goal of this simulation was to detect potential specific H_2O/p-RNA interactions which might strongly alter the behavior of the duplex as compared to the simple continuum solvent model.

REFERENCES

[1] R. Krishnamurthy, S. Pitsch, M. Minton, C. Miculka, N. Windhab, A. Eschenmoser, *Angew. Chem.* **1996,** *108,* 1619; *ibid. Int. Ed.* **1996,** *35,* 1537.

[2] S. Pitsch, S. Wendeborn, B. Jaun, A. Eschenmoser, *Helv. Chim. Acta* **1993,** *76,* 2161.

[3] S. Pitsch, R. Krishnamurthy, M. Bolli, S. Wendeborn, A. Holzner, M. Minton, C. Lesueur, I. Schlönvogt, B. Jaun, A. Eschenmoser, *Helv. Chim. Acta* **1995,** *78,* 1621.

[4] A. Eschenmoser, M. Dobler, *Helv. Chim. Acta* **1992,** *75,* 218.

[5] A. Eschenmoser, 'Toward a chemical ethiology of the natural nucleic acids' structure', Proceedings of The Robert A. Welch Foundation 37th Conference on Chemical Research, '40 Years of the DNA Double Helix', Houston, Texas, 1993, p. 201.

[6] G. Otting, M. Billeter, K. Wüthrich, H.-J. Roth, C. Leumann, A. Eschenmoser, *Helv. Chim. Acta* **1993,** *76,* 2701.

[7] J. Hunziker, H.-J. Roth, M. Böhringer, A. Giger, U. Diederichsen, M. Göbel, R. Krishnan, B. Jaun, C. Leumann, A. Eschenmoser, *Helv. Chim. Acta* **1993,** *76,* 259.

[8] J. Hunziker, Thesis, ETH No. 9814, 1992.

[9] K. Wüthrich, 'NMR of Proteins and Nucleic Acis', Wiley-Interscience, New York, 1986.

[10] S. S. Wijmenga, M. M. W. Mooren, C. W. Hilbers, in 'NMR of Macromolecules. A Practical Approach', Ed. G. C. K. Roberts, The Practical Approach Series, Eds. D. Rickwood and B. D. Hames, Vol. 134, p. 217.

[11] U. Schmitz, T. L. James, in 'Nuclear Magnetic Resonance and Nucleic Acids', Ed. T. L. James, Methods in Enzymology, Vol. 261, Academic Press, San Diego, 1995, p. 3.

[12] G. Varani, F. Aboul-ela, F. H.-T. Allain, *Prog. Nucl. Magn. Reson.* **1996,** *29,* 51.

[13] C. Altona, C. A. G. Haasnoot, *Org. Magn. Reson.* **1980,** *13,* 417.
[14] IUPAC-IUB, Joint Commission on Biochemical Nomenclature, *Eur. J. Biochem.* **1983,** *131,* 9.
[15] G. M. Clore, A. M. Gronenborn, *J. Magn. Reson.* **1985,** *61,* 158.
[16] D. Neuhaus, M. Williamson, 'The Nuclear Overhauser Effect in Structural and Conformational Analysis', VCH Publishers, Weinheim, 1989.
[17] C. Giessner-Prettre, B. Pullman, *Biopolymers* **1976,** *15,* 2277.
[18] C. Giessner-Prettre, B. Pullman, *Biochem. Biophys. Res. Commun.* **1976,** *70,* 578.
[19] M. Guéron, J.-L. Leroy, in 'Nuclear Magnetic Resonance and Nucleic Acids', Ed. T. L. James, Methods in Enzymology, Vol. 261, Academic Press, San Diego, 1995, Vol. 261, p. 383.
[20] B. McConnell, *J. Biomol. Struct. Dyn.* **1984,** *1,* 1407.
[21] S. Pitsch, S. Wendeborn, R. Krishnamurthy, A. Holzner, M. Minton, C. Miculka, M. Bolli, A. Eschenmoser, *Helv. Chim. Acta,* in preparation.
[22] Y. Hayakawa, S. Wakabayashi, H. Kato, R. Noyori, *J. Am. Chem. Soc.* **1990,** *112,* 1691.
[23] 'Thermodynamic data for Biochemistry and Biotechnology', Ed. K. J. Breslauer, Springer Verlag, Berlin, 1986, p. 402ff.
[24] D. De Prisco Albergo, L. A. Marky, K. J. Breslauer, D. H. Turner, *Biochemistry* **1981,** *20,* 1409.
[25] L. A. Marky, K. J. Breslauer, *Biopolymers* **1987,** *26,* 1601.
[26] A. Derome, M. Williamson, *J. Magn. Reson.* **1990,** *88,* 177.
[27] S. P. Rucker, A. J. Shaka, *Mol. Phys.* **1989,** *68,* 509.
[28] C. Griesinger, R. R. Ernst, *J. Magn. Reson.* **1987,** *75,* 261.
[29] S. Macura, R. R. Ernst, *Mol. Phys.* **1980,** *41,* 95.
[30] V. Sklenar, H. Miyashiro, G. Zon, H. T. Miles, A. Bax, *FEBS Lett.* **1986,** *208,* 94.
[31] A. L. Davis, J. Keeler, E. D. Laue, D. Moskau, *J. Magn. Reson.* **1992,** *98,* 207.
[32] M. Piotto, V. Saudek, V. Sklenar, *J. Magn. Reson. Series A* **1993,** *102,* 241.
[33] M. Piotto, V. Saudek, V. Sklenar, *J. Biomol. NMR* **1992,** *2,* 661.
[34] S. J. Weiner, P. A. Kollman, D. T. Nguyen, D. A. Case, *J. Comput. Chem.* **1986,** *7,* 230.
[35] H. J. C. Berendsen, P. M. Postma, W. F. van Gunsteren, A. DiNola, J. R. Haak, *J. Chem. Phys.* **1984,** *81,* 3684.
[36] U. C. Singh, S. J. Weiner, P. A. Kollman, *Proc. Natl. Acad. Sci. U.S.A.* **1985,** *82,* 755.
[37] W. L. Jorgensen, J. Chandrasekhar, J. D. Madura, R. W. Impey, M. L. Klein, *J. Phys. Chem.* **1983,** *79,* 926.